Mode-III fatigue of welded joints in steel maritime structures

Weld notch shear stress distributions and effective notch stress based resistance

Bufalari, Gabriele; den Besten, Henk; Kaminski, Miroslaw Lech

DOI
10.1016/j.ijfatigue.2022.107210

Publication date
2022

Document Version
Final published version

Published in
International Journal of Fatigue

International Journal of Fatigue 165 (2022) 107210

Contents lists available at ScienceDirect

International Journal of Fatigue

journal homepage: www.elsevier.com/locate/ijfatigue

Mode-III fatigue of welded joints in steel maritime structures: Weld notch shear stress distributions and effective notch stress based resistance

Gabriele Bufalari, Henk den Besten *, Miroslaw Lech Kaminski

Maritime and Transport Technology Department, Delft University of Technology, Delft, The Netherlands

ARTICLE INFO

Keywords:
Fatigue
Mode-III
Welded joints
Stress distribution
Effective notch stress

ABSTRACT

The predominant mode-I response of maritime structures can be multiaxial, involving out-of-plane mode-III shear components. Semi-analytical mode-III notch stress distribution formulations have been established for critical details like welded T-joints and cruciform joints, reflecting (non-)symmetry with respect to half the plate thickness. Using a stress distribution formulation based effective notch stress as fatigue strength criterion, the mode-III welded joint mid-cycle fatigue resistance characteristics have been investigated. In comparison to mode-I, the material characteristic length and resistance curve slope estimate suggest the fatigue damage process to be even more an initiation related near-surface phenomenon. Mean shear stress effects seem insignificant.

1. Introduction

Maritime structures like offshore support vessels and floating offshore wind turbines (Fig. 1) are exposed to cyclic loading, both environment (wind, waves) and service (machinery) induced, introducing a cyclic response. Fatigue can be a governing limit state [1]. Fatigue sensitive locations in plane geometries appear at material scale in micro- and meso-scopic stress concentrations. In notched geometries, fatigue sensitive locations emerge at structural scale in macro-scopic stress concentrations; hot spots facilitating micro- and meso- scopic ones [2], either as part of structural members (e.g. cut-outs) or at structural member connections (e.g. joints). Maritime structures are traditionally structural member assemblies in reinforced panel- or truss/frame-setup; i.e. planar or tubular structures. For commonly applied materials like steel, the arc-welded joints typically connecting the structural members are fatigue sensitive.

In general, maritime structural response conditions can be multiaxial, involving normal mode-I, in-plane shear mode-II and/or out-of-plane mode-III shear components (Fig. 2) with potential contributions from loading, geometry and/or even material sources. Environmental – external – loading, like sea and swell, can come from different directions. Stiffness variations because of changing geometry or material anisotropy (e.g. in case of polymer composites) enable multiple – internal – load transfer mechanisms along dissimilar paths. The (curved) structural member plate thickness is often relatively small in comparison to the width and length. Since the governing external environmental loading, water and cargo pressure, is a distributed one, the normal force F_n as well as the in-plane and out-of-plane bending moments, $M_{b,ip}$ and $M_{b,op}$ – internal mode-I loading components – are typically significant. At the same time, the in-plane shear force $F_{s,ip}$ mode-II contribution is negligible. However, the out-of-plane shear force $F_{s,op}$ and torsion moment M_t mode-III components affect in specific cases [3,4] the predominant mode-I response and multiaxiality has to be taken into account for accurate fatigue strength and life time estimates [e.g.5].

The fatigue damage process involves initiation and growth contributions [1] and can be modelled adopting respectively intact and cracked geometry parameters [2]. Although for welded joints crack growth dominates, the fatigue life time N is predominantly spent in the notch affected region [6], meaning a notch characteristic intact geometry parameter rather than a cracked geometry one can be adopted as fatigue strength criterion.

Far field response spectra of welded joints in steel maritime structures are predominantly linear elastic, explaining why the fatigue strength criterion S is typically of the stress – rather than strain or energy – type and particularly related to mid- and high-cycle fatigue [7].

The through-thickness weld toe and weld root notch stress distributions along the expected (2D) crack path are assumed to be a key element in defining an appropriate fatigue design and detectable repair criterion [8]. Analytical expressions have already been established for mode-I [7–9], related to the welded joint far field stress as typically can

* Corresponding author.
E-mail address: Henk.denBesten@tudelft.nl (H. den Besten).

https://doi.org/10.1016/j.ijfatigue.2022.107210
Received 20 April 2022; Received in revised form 9 August 2022; Accepted 12 August 2022
Available online 17 August 2022

Nomenclature

Symbols

α	(half) notch angle
β	particular stress angle
γ	loading & response ratio coefficient
Δ	prefix indicating stress range
ϵ	residual
θ	generic stress angle
λ	eigenvalue
λ_τ	first mode-III eigenvalue
μ	mean
$\mu_{\tau F}$	force equilibrium coefficient
$\mu_{\tau M}$	moment equilibrium coefficient
ρ	(real) weld notch radius
ρ^*	material characteristic length
σ	(fatigue life time) standard deviation
τ_e	effective notch shear stress
τ_{fe}	(equilibrium equivalent) linear structural field stress
$\tau_n\ (r/t_p)$	weld toe notch shear stress distribution
τ_{nom}	nominal shear stress
τ_{ns}	pure shear force induced τ_n
τ_{nt}	pure torsion moment induced τ_n
τ_s	structural shear stress
τ_{se}	self equilibrium stress
τ_{ss}	f_s induced structural shear stress component
τ_{st}	m_t induced structural shear stress component
τ_{tw}	weld load carrying shear stress
$\boldsymbol{\Phi}$	parameter vector
C	fatigue resistance curve intercept
C_{tw}	weld load carrying shear stress coefficient
F_s	nodal shear force
f_s	line shear force
h_w	weld leg height
l_w	weld leg length
m	fatigue resistance curve slope
M_t	nodal torsion moment
m_t	line torsion moment
N	fatigue lifetime in number of cycles
O	coordinate system origin
r_0	radial distance of coordinate system origin to notch tip
R	loading & response ratio
r	radial coordinate
r_{τ_s}	structural shear stress ratio
R_t	tube outer radius
S	fatigue strength criterion
S_e	effective notch stress criterion
S_n	nominal stress criterion
t_b	base plate thickness
t_c	cross plate thickness
t_p	plate thickness
$T_{\sigma S_n}$	10%–90% strength scatter band index
$\mathcal{L}$	log-likelihood
$\hat{}$	circumflex indicating parameter MLE

Abbreviations

DS	double side
FE	finite element
MLE	maximum likelihood estimate

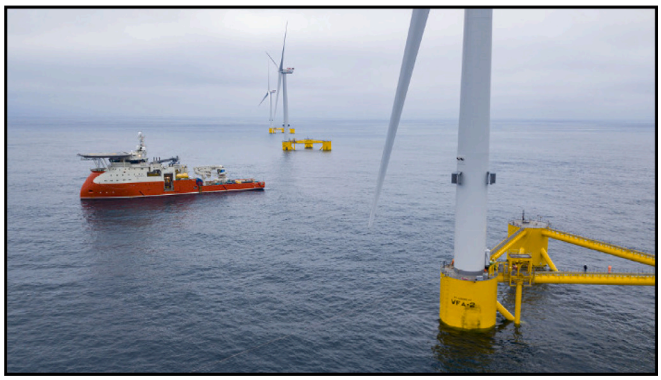

Fig. 1. Support vessel and wind turbine, respectively a planar and tubular maritime structure.

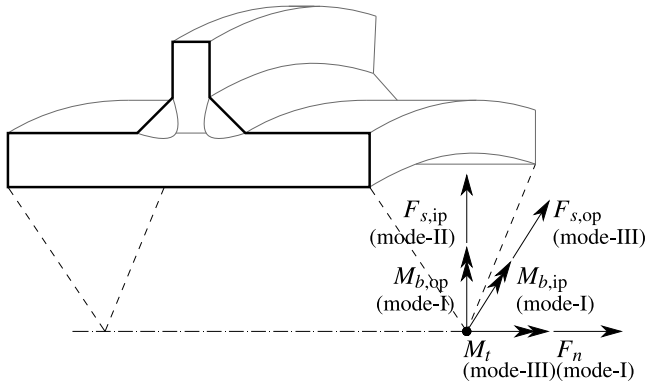

Fig. 2. DS welded T-joint in a tubular structure with internal load components.

be obtained using relatively coarse meshed shell/plate finite element (FE) models. However, expressions for mode-III are not available yet and will be established for weld toe notches in double side (DS) welded T-joints and DS welded cruciform-joints, reflecting respectively non-symmetry and symmetry with respect to half the plate thickness (Section 2).

Different fatigue assessment concepts, relating the fatigue life time N and a fatigue strength criterion S using a resistance curve, have been developed over time aiming to obtain more accurate life time estimates, balanced with criterion complexity and computational efforts [8]. Incorporating local (notch) information provides more generalised S formulations and the number of involved fatigue resistance curves reduces accordingly (i.e. ultimately to one), like for the effective notch stress concept [8,10–15]. Taking advantage of the weld notch stress distribution expressions, the effective notch stress S_e can be calculated averaging the notch stress distribution along the expected crack path over a material characteristic length ρ^*, meaning solid FE models to estimate S_e are not required anymore. Following mode-I investigations [7,8], a mode-III mid-cycle fatigue S_e-N curve will be established for welded joints in steel structures (Section 3), paying particular attention to the material characteristic length since ρ^* seems never been investigated before.

2. Mode-III weld toe notch shear stress distributions

In order to capture the mode-III through-thickness weld toe notch shear stress distributions $\tau_n(r/t_p)$ along the expected (2D) crack path with plate thickness t_p either the base plate or cross plate value, t_b or t_c, the welded joint far field response is assumed to be linear elastic. Adopting a linear superposition principle [9] a far field related equilibrium equivalent and self-equilibrium part will be distinguished, τ_{fe} and

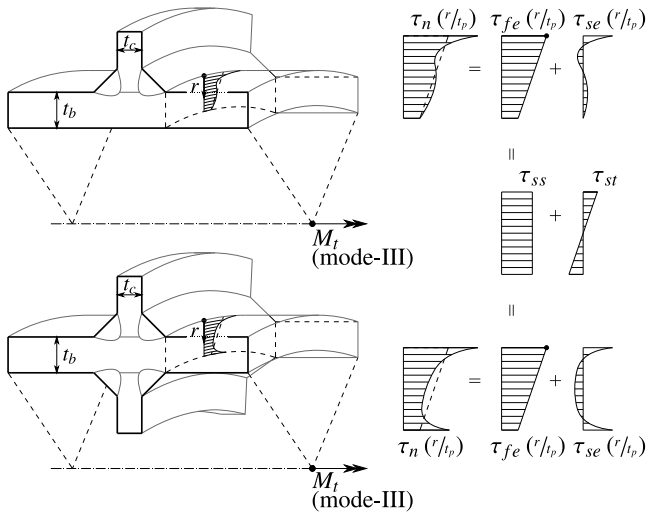

Fig. 3. Linear superposition of an equilibrium equivalent and self-equilibrium part for the mode-III weld toe notch shear stress distribution of a DS welded T-joint and DS welded cruciform joint.

τ_{se} (Fig. 3) involving three components: the notch stress (Section 2.1), the weld-load carrying stress (Section 2.2) and the far field stress (Section 2.3). Formulations will be derived for both non-symmetry (Section 2.4) and symmetry (Section 2.5) with respect to half the plate thickness ($t_p/2$), using respectively a DS welded T-joint and DS welded cruciform joint for illustration purposes, in case of both zero and finite notch radius ρ. Please note that the cruciform joint in IIW standard [16] and Eurocode [17] is referred to as two-sided transverse attachment, considering both the geometry and loading applied at the continuous member. The adopted joint annotation is based on geometry only, since the variety in loading conditions can be large, in particular in case of multiaxiality.

2.1. Notch stress component

The singular stress distribution at a V-shaped notch for a fillet weld geometry with $\rho = 0$ (Fig. 4) can be obtained [18–22] assuming symmetry with respect to the notch bisector ($\theta = 0$). A tangential component formulation for a particular stress angle ($\theta = \beta$) has been established Appendix A, including a relation to the far field stress parameter τ_s (Section 2.3):

$$\tau_{x\theta}\left(\frac{r}{t_p}\right) = \tau_s\left(\frac{r}{t_p}\right)^{\lambda_\tau - 1} \mu_{\tau F}\cos(\lambda_\tau \beta) \tag{1}$$

with

$$\mu_{\tau F} = \frac{C_1' t_p^{\lambda_\tau - 1}}{\tau_s} \tag{2}$$

and

$$\lambda_\tau = \frac{\pi}{2\alpha}. \tag{3}$$

Although the real weld notch radius ρ is often virtually zero – justifying the $\rho = 0$ assumption, in some cases the influence of $\rho > 0$ (Fig. 5) cannot be neglected. The coordinate system origin will be transformed ($O' \rightarrow O$), keeping the Polar axis parallel to the original one:

$$r'^2 = r^2 + 2\cos(\beta - \theta)\, r_0 r + r_0^2 \tag{4}$$

with

$$r_0 = \rho\left(1 - \frac{\pi}{2\alpha}\right). \tag{5}$$

For a particular stress angle $\theta = \beta$, the tangential component becomes Appendix A:

$$\tau_{x\theta}\left(\frac{r}{t_p}\right) = \tau_s\left(\frac{r'}{t_p}\right)^{\lambda_\tau - 1} \mu_{\tau F}\cos(\lambda_\tau \beta)\left\{1 + \left(\frac{r_0}{t_p}\right)^{2\lambda_\tau}\left(\frac{r'}{t_p}\right)^{-2\lambda_\tau}\right\} \tag{6}$$

Comparing $\tau_{x\theta}(r/t_p)$ for zero and finite notch radius (Eqs. 1 and 6), the ($\rho = 0$) formulation is basically the ($\rho > 0$) limit case. In contrast to the mode-I formulation [7–9], only one singular term is involved rather than two.

2.2. Weld load carrying stress component

The weld geometry causes a local change in stiffness, meaning the centre of twist varies from section to section along the y-axis (Fig. 6). Each welded joint section is basically a rectangle containing two axes of symmetry, meaning the centre of twist is located at the intersection and coincides at the same time with the centroid. Connecting the centres of twist of each section introduces the elastic axis (Fig. 6) and coincides with the neutral axis. A torsion moment induced linear shear stress distribution $\tau_{tw}(r/t_p)$ appears and the weld becomes load carrying up to some extent. Considering a weld toe notch as typically encountered in a partial penetrated DS welded T-joint at the base plate without symmetry with respect to ($t_p/2$), the torsion moment is counter-clockwise for f_s pointing in x-direction and counter-clockwise m_t in the

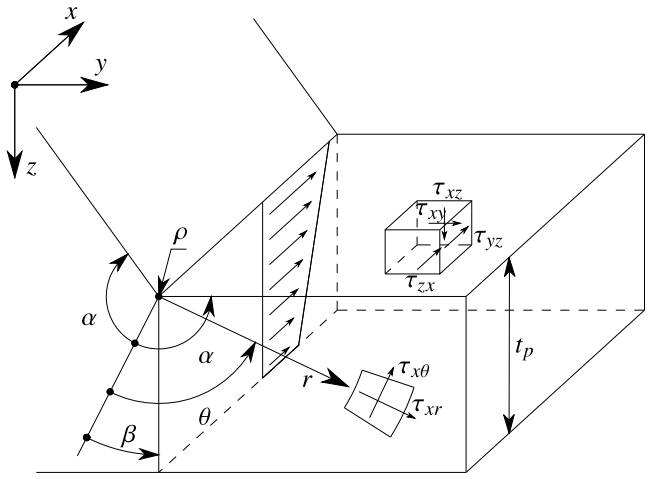

Fig. 4. Notch stress components in Cartesian and Polar coordinates for $\rho = 0$.

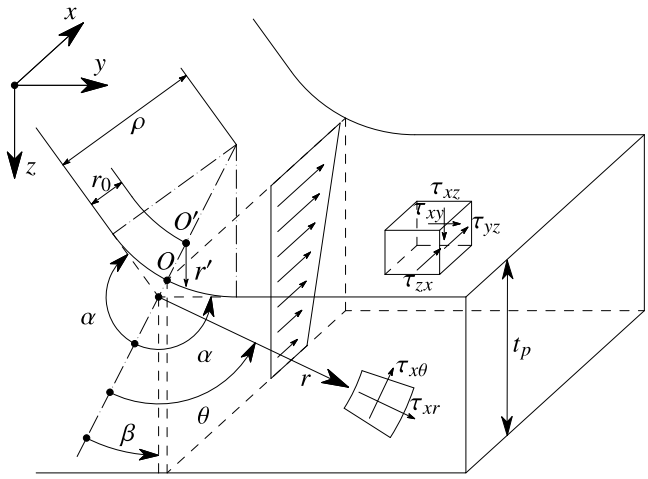

Fig. 5. Notch stress components in Cartesian and Polar coordinates for $\rho > 0$.

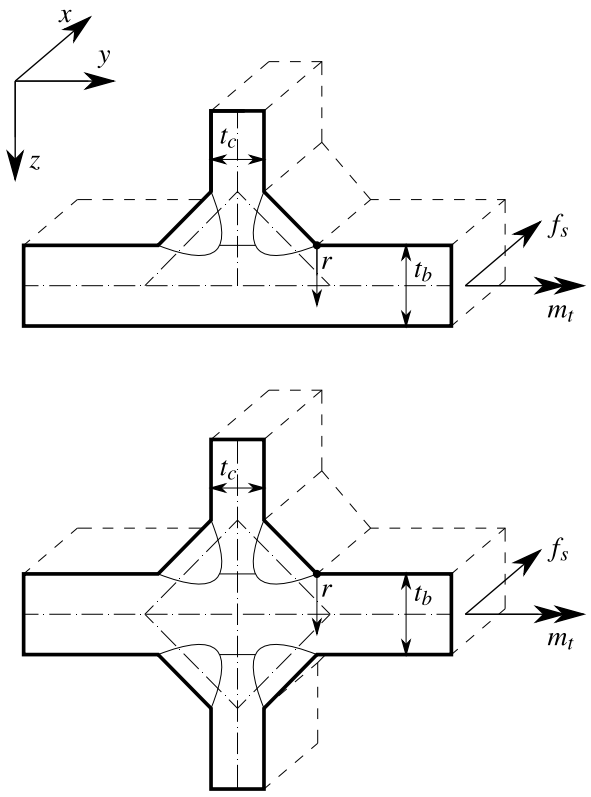

Fig. 6. Weld geometry induced shift of centre of twist for the non-symmetry and symmetry case.

x-z plane and the weld load carrying (shear) stress distribution yields:

$$\tau_{tw}\left(\frac{r}{t_p}\right) = \tau_s C_{tw}\left\{2\left(\frac{r}{t_p}\right) - 1\right\} \text{ for } \{0 \le \left(\frac{r}{t_p}\right) \le 1\}. \tag{7}$$

The far field stress (Section 2.3) related magnitude $\tau_s C_{tw}$ is geometry and loading dependent. If symmetry with respect to $(t_p/2)$ is detected, like for a DS welded cruciform joint (Fig. 6), the $\tau_{tw}(r/t_p)$ distribution is based on half the plate thickness only:

$$\tau_{tw}\left(\frac{r}{t_p}\right) = \tau_s C_{tw}\left\{4\left(\frac{r}{t_p}\right) - 1\right\} \text{ for } \{0 \le \left(\frac{r}{t_p}\right) \le 1\}. \tag{8}$$

2.3. Far field stress component

The linear structural field stress distribution $\tau_{fe}(r/t_p)$ in the cross-section at a weld toe (Fig. 3), in compliance with the fracture mechanics defined far field stress [23,24], is characterised using the structural shear stress τ_s and structural shear stress ratio r_{τ_s}:

$$\tau_{fe}\left(\frac{r}{t_p}\right) = \tau_s\left\{1 - 2r_{\tau_s}\left(\frac{r}{t_p}\right)\right\} \text{ for } \{0 \le \left(\frac{r}{t_p}\right) \le 1\}. \tag{9}$$

A relatively coarse meshed shell/plate FE model is typically sufficient to estimate the far-field stress of welded joints in maritime structures [25,26], naturally embedding the constant membrane (mode-I)/shear (mode-III) and linear bending (mode-I)/torsion (mode-III) components [27]. If the welded joint structural stiffness – either in planar or tubular structures – does not significantly affect the stress distribution, like in general for groove welds (e.g. in butt joints), the weld does not need to be modelled and the far field stress information can be obtained at the intersection line of the connected structural members [28]. However, if weld modelling is required – like often for fillet welds (e.g. in T-joints and cruciform joints), several options are available including inclined shell elements, inclined rigid elements or shell elements with increased local thickness at the joint location [29]. For the considered mode-III loading & response conditions, inclined shell element modelling has been adopted (Fig. 7) as it seems to be most convenient in engineering practice [27]. Transforming the nodal shear forces $F_{s,i}$ and torsion moments $M_{t,i}$ along the weld seam to line forces and moments $f_{s,i}$ and $m_{t,i}$, $\{F_s\} = [T]\{f_s\}$ and $\{M_t\} = [T]\{m_t\}$ [24,30,31], the shear force and torsion moment induced structural stress components τ_{ss} and τ_{st} can be calculated to obtain the structural shear stress:

$$\tau_s = \tau_{ss} + \tau_{st} \tag{10}$$

with

$$\tau_{ss} = f_s/t_p \tag{11a}$$

$$\tau_{st} = 6m_t/t_p^2. \tag{11b}$$

The structural shear stress ratio $(-\infty < r_{\tau_s} \le 1)$ represents the relative contribution of τ_{st} to τ_s, i.e. the far field stress gradient:

$$r_{\tau_s} = \tau_{st}/\tau_s. \tag{12}$$

Rewriting τ_{ss} and τ_{st} in terms of τ_s (Eq. 10) and r_{τ_s} (Eq. 12) yield:

$$\tau_{ss} = \tau_s(1 - r_{\tau_s}) \tag{13a}$$

$$\tau_{st} = r_{\tau_s}\tau_s. \tag{13b}$$

2.4. Stress distribution for non-symmetry with respect to $(t_p/2)$

Using the notch stress component $\tau_{x\theta}$ (Eq. 1), the weld load carrying stress τ_{tw} (Eq. 7) and structural field stress formulation τ_{fe} (Eq. 9), the mode-III stress distribution for the non-symmetry case (Fig. 8) – along the (2D) crack path – can be obtained for $\rho = 0$:

$$\tau_n\left(\frac{r}{t_p}\right) = \tau_s\left[\left(\frac{r}{t_p}\right)^{\lambda_\tau - 1}\mu_{\tau F}\cos(\lambda_\tau\beta) - (C_{tw} + \mu_{\tau M})\left\{2\left(\frac{r}{t_p}\right) - 1\right\} - 2r_{\tau_s}\left(\frac{r}{t_p}\right)\right]. \tag{14}$$

The self-equilibrium stress part $\tau_{se} + 1$, $(r/t_p)^{\lambda_\tau - 1}\mu_{\tau F}\cos(\lambda_\tau\beta) - (C_{tw} + \mu_{\tau M})\{2(r/t_p) - 1\}$ is scaled and projected – using τ_s and r_{τ_s} – onto the structural field stress. For $r_{\tau_s} > 0$ the stress distribution will be

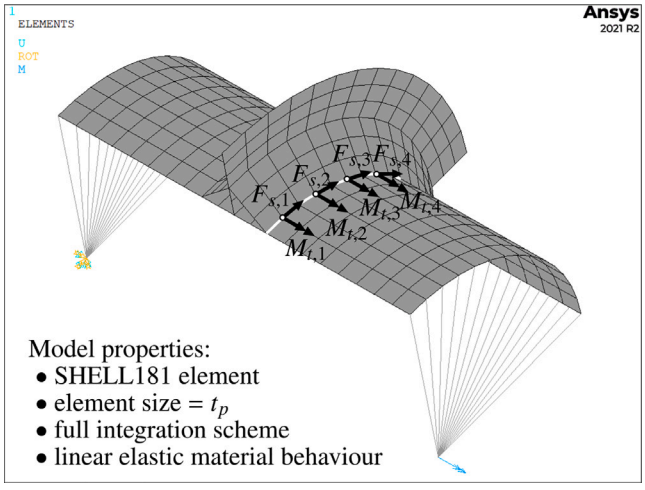

Fig. 7. Part of a shell FE model of a (non-symmetric) T-joint in a tubular structure.

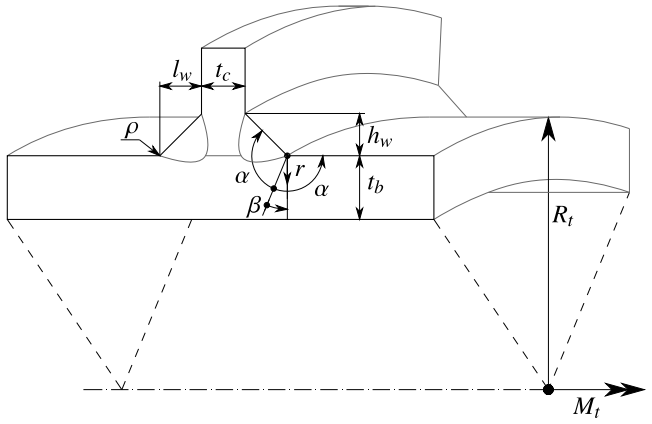

Fig. 8. DS welded T-joint showing non-symmetry with respect to $(t_b/2)$, either in a tubular or planar $(R_t \to \infty)$ structure.

monotonic; in case $r_{\tau_s} \leq 0$ non-monotonic. Involving $\tau_{x\theta}$ (Eq. 6), the distribution for $\rho > 0$ can be obtained as well:

$$\tau_n\left(\frac{r}{t_p}\right) = \tau_s\left[\left(\frac{r'}{t_p}\right)^{\lambda_\tau - 1}\mu_{\tau F}\cos(\lambda_\tau\beta)\left\{1 + \left(\frac{r_0}{t_p}\right)^{2\lambda_\tau}\left(\frac{r'}{t_p}\right)^{-2\lambda_\tau}\right\} - (C_{tw} + \mu_{\tau M})\left\{2\left(\frac{r'}{t_p}\right) - 1\right\} - 2r_{\tau_s}\left(\frac{r'}{t_p}\right)\right]. \tag{15}$$

Although principally the notch stress component in Cartesian coordinates is required, a transformation (Eq. A.2) does not affect the formulation: $\tau_{xz} = \tau_{xr}\cos(\theta) - \tau_{x\theta}\sin(\theta) = \tau_s(r/t_p)^{\lambda_\tau - 1}\mu'_{\tau F}\cos(\lambda_\tau\beta)$ for $\rho = 0$, explaining why $\tau_{x\theta}$ (Eq. 1) has been used. The involved eigenvalue λ_τ (Fig. A.29) and the stress angle $\beta = (\alpha - \pi/2)$ are notch angle α dependent. For fillet welds (Fig. 8):

$$\alpha = \frac{1}{2}\left\{\pi + \arctan\left(\frac{h_w}{l_w}\right)\right\}. \tag{16}$$

Like for the mode-I formulation [7–9], two constants are required in order to satisfy both force and moment equilibrium. Since just one constant $\mu_{\tau F}$ is naturally available – comparable to the symmetric mode-I term – a linear anti-symmetric term $-\mu_{\tau M}\{2(r/t_p) - 1\}$ has been introduced to be able to achieve self-equilibrium. Rather than solving the system of force and moment equilibrium equations for $\mu_{\tau F}$ and $\mu_{\tau M}$, like for mode-I, the two equations can be solved sequentially since force equilibrium is identically satisfied for the anti-symmetric term. Force equilibrium in a weak form:

$$\int_0^1 \tau_n\left(\frac{r}{t_p}\right)\mathrm{d}\left(\frac{r}{t_p}\right) = \int_0^1 \tau_s\left\{1 - 2r_{\tau_s}\left(\frac{r}{t_p}\right)\right\}\mathrm{d}\left(\frac{r}{t_p}\right) \tag{17}$$

provides for $\rho = 0$

$$\mu_{\tau F} = \frac{\lambda_\tau}{\cos(\lambda_\tau\beta)}. \tag{18}$$

For $\rho > 0$ the coordinate system transformation (Eqs. 4 and 5) becomes involved and force equilibrium in weak form:

$$\int_{\left(\frac{r_0}{t_p}\right)}^1 \tau_n\left(\frac{r}{t_p}\right)\mathrm{d}\left(\frac{r}{t_p}\right) = \int_0^1 \tau_s\left\{1 - 2r_{\tau_s}\left(\frac{r}{t_p}\right)\right\}\mathrm{d}\left(\frac{r}{t_p}\right) \tag{19}$$

with

$$\frac{r_0}{t_p} = \frac{\rho}{t_p}\left(1 - \frac{\pi}{2\alpha}\right) \tag{20}$$

provides

$$\mu_{\tau F} = -\frac{\lambda_\tau\left\{\mu_{\tau M}\left[\left(\frac{r_0}{t_p}\right)^2 - \left(\frac{r_0}{t_p}\right)\right] - \left(\frac{r_0}{t_p}\right)^2 r_{\tau_s} - 1\right\}}{\cos(\lambda_\tau\beta)\left[1 - \left(\frac{r_0}{t_p}\right)^{2\lambda_\tau}\right]}. \tag{21}$$

Note that with the obtained $\mu_{\tau F}$ formulation $\tau_n(r/t_p)$ turns out to be stress angle β independent. Moment equilibrium in a weak form for $\rho = 0$:

$$\int_0^1 \tau_n\left(\frac{r}{t_p}\right)\cdot\left(\frac{r}{t_p}\right)\mathrm{d}\left(\frac{r}{t_p}\right) = \int_0^1 \tau_s\left\{1 - 2r_{\tau_s}\left(\frac{r}{t_p}\right)\right\}\left(\frac{r}{t_p}\right)\mathrm{d}\left(\frac{r}{t_p}\right) \tag{22}$$

yields $\mu_{\tau M} = \{3(\lambda_\tau - 1) + C_{tw}(\lambda_\tau + 1)\}/(\lambda_\tau + 1)$. However, substitution in $\tau_n(r/t_p)$ provides a C_{tw} independent equation, since the introduced anti-symmetric term and the weld load carrying stress have the same form. Ignoring the weld load carrying stress contribution denotes:

$$\mu_{\tau M} = \frac{3(\lambda_\tau - 1)}{(\lambda_\tau + 1)}. \tag{23}$$

For $\rho > 0$ the same considerations apply:

$$\int_{\left(\frac{r_0}{t_p}\right)}^1 \tau_n\left(\frac{r}{t_p}\right)\cdot\left(\frac{r}{t_p}\right)\mathrm{d}\left(\frac{r}{t_p}\right) = \int_0^1 \tau_s\left\{1 - 2r_{\tau_s}\left(\frac{r}{t_p}\right)\right\}\left(\frac{r}{t_p}\right)\mathrm{d}\left(\frac{r}{t_p}\right) \tag{24}$$

providing

$$\mu_{\tau M} = \frac{\begin{array}{c} 6\lambda_\tau(\lambda_\tau + 1)\left(\frac{r_0}{t_p}\right)^{2\lambda_\tau+1} - 3(\lambda_\tau^2 - 1)\left(\frac{r_0}{t_p}\right)^{2\lambda_\tau+2} - \\ 12\lambda_\tau\left(\frac{r_0}{t_p}\right)^{\lambda_\tau+2} - 3(\lambda_\tau + 1)^2\left(\frac{r_0}{t_p}\right)^{2\lambda_\tau} + 12\lambda_\tau\left(\frac{r_0}{t_p}\right)^{\lambda_\tau+1} + \\ 3\left[\left(\frac{r_0}{t_p}\right) - 1\right](\lambda_\tau - 1)\left\{\left[\left(\frac{r_0}{t_p}\right) - 1\right]\lambda_\tau + \left(\frac{r_0}{t_p}\right) + 1\right\} \end{array}}{\begin{array}{c} 6\lambda_\tau(\lambda_\tau + 1)\left(\frac{r_0}{t_p}\right)^{2\lambda_\tau+1} - (9\lambda_\tau^2 + 6\lambda_\tau - 3)\left(\frac{r_0}{t_p}\right)^{2\lambda_\tau+2} - \\ 12\lambda_\tau\left(\frac{r_0}{t_p}\right)^{\lambda_\tau+2} - (\lambda_\tau^2 - 1)\left(\frac{r_0}{t_p}\right)^{2\lambda_\tau} + 12\lambda_\tau\left(\frac{r_0}{t_p}\right)^{\lambda_\tau+3} + \\ \left\{\left[-4\left(\frac{r_0}{t_p}\right)^3 + 9\left(\frac{r_0}{t_p}\right)^2 + 4\left(\frac{r_0}{t_p}\right)^{2\lambda_\tau+3} - 6\left(\frac{r_0}{t_p}\right) + 1\right]\lambda_\tau - \right. \\ \left. 4\left(\frac{r_0}{t_p}\right)^3 + 3\left(\frac{r_0}{t_p}\right)^2 + 4\left(\frac{r_0}{t_p}\right)^{2\lambda_\tau+3} + 1\right\}(\lambda_\tau - 1) \end{array}}. \tag{25}$$

The $\mu_{\tau F}$ and $\mu_{\tau M}$ expressions obtained for $\rho = 0$ are basically $\rho > 0$ limit values. Although moment equilibrium is not exactly satisfied since the weld load carrying stress has been ignored, at least $\tau_s C_{tw}\{2(r/t_p) - 1\}$ is still part of $\tau_n(r/t_p)$ to take care of the welded joint geometry and loading dependent weld notch stress contributions.

The weld load carrying stress magnitude $\tau_s C_{tw}$ is assumed to be a linear superposition of a shear force f_s and torsion moment m_t induced component, meaning C_{tw} is r_{τ_s} dependent. For a tubular structure with attachment involving a DS welded T-joint and exposed to a torsion moment M_t (Fig. 8), the structural stress ratio r_{τ_s} changes for varying ratio of tube radius R_t and thickness t_p. For the limit cases, respectively $R_t \to t_b$ (corresponding to a solid shaft) and $R_t \to \infty$ (corresponding to a quasi-planar structure), the pure torsion and pure shear case appear. However, the pure torsion case introduces geometrical symmetry at the same time. Investigating the relative load path contributions using a 2D axisymmetric FE model (Fig. 14), the pure shear case will be considered to identify the weld load carrying mechanism for non-symmetry with respect to $(t_p/2)$. If a torsion moment is applied to the tube with $R_t \to \infty$ (Fig. 8), the DS welded T-joint contains two parallel load paths: one through the base plate and one through the weld and cross plate. The shear stiffness and torsion stiffness of the load paths define

how the loading is divided. The base plate load path related shear stiffness dominates generally speaking the weld and cross plate load path related torsion stiffness, explaining the $(f_{s,t_b}/f_s)$ values closer to 1 (Fig. 9). For increasing t_b, the shear force through the base plate increases because of increasing base plate load path stiffness. The weld and cross plate load path torsion stiffness increases for increasing t_c, l_w, and h_w, meaning the base plate load path contribution decreases. The considered range of dimensions is representative for maritime structures consisting of structural members with relatively small plate thickness in comparison to the width and length.

In order to obtain the required C_{tw} values, FE solutions and analytical results (Eq. 14) for a range of geometry dimensions have been used to establish a 4th order polynomial fitting function (Eq. B.1). Geometry contributions – including the notch angle (l_w/h_w) – and two load path parameters: (l_w/t_b) and the log-ratio of $(t_c/2 + l_w)/t_b$ are involved, as well as (t_b/R_i) implicitly representing the internal loading contribution in terms of r_{τ_s} Appendix B. The weld load carrying stress turns out to be virtually ρ independent for realistic values: $(\rho/t_b) \leq 0.2$, and has been neglected in establishing the C_{tw} fitting function.

Comparing the required C_{tw} values to the estimates (Fig. 10) reflect a good match. Depending on the joint dimensions, the weld load carrying stress level for the weld toe notch at the base plate can be up to about 30 [%] of the structural stress τ_s. For varying t_b, t_c, and h_w, the trends are the same and opposite to the relative base plate loads (Fig. 9) as expected because of the same physics. Increasing t_b decreases C_{tw} since the relative stiffness contribution of the weld and cross plate load path decreases. For increasing t_c and h_w, the C_{tw} values increase because the relative weld and cross plate load path stiffness increases. For increasing l_w, the load through the base plate decreases; the load through the weld and cross plate increases accordingly. However, C_{tw} decreases for increasing l_w, meaning the weld notch becomes less effective. Asymptotically decreasing C_{tw} behaviour – related to the pure shear limit case $(r_{\tau_s} = 0)$ – can be observed for increasing R_i, meaning C_{tw} is relatively small in comparison to the pure torsion case $(r_{\tau_s} = 1)$.

A monotonic through-thickness stress distribution at the weld toe notch of the base plate is shown (Fig. 11) for a combined load case $(r_{\tau_s} = 0.24)$; the torsion moment is applied counter-clockwise. A non-monotonic one is shown (Fig. 12) for a pure shear force $(r_{\tau_s} = 0)$. The joint dimensions are arbitrary, but realistic for maritime structures. A comparison of the weld toe notch stress- and far field stress distributions indicate that force and moment equilibrium is (approximately) satisfied indeed. Converged solid FE model solutions (Fig. 14) are added for comparison (Figs. 11 and 12), showing that the semi-analytical $\tau_n(r/t_p)$ formulations (Eqs. 14 and 15) provide accurate stress distributions. In general, the relative error (Fig. 13) – obtained considering all stress distributions for the full parameter range – is within 5 [%]. Like for the mode-I formulations, three zones can be identified: the zone 1 peak stress value, the zone 2 notch-affected stress gradient and the zone 3 far-field dominated stress gradient, demonstrating stress field similarity.

2.5. Stress distribution for symmetry with respect to $(t_p/2)$

Weld toe notches appear at both sides of a plate/shell if stress distribution symmetry with respect to $(t_p/2)$ is detected, as shown for a DS welded cruciform joint (Fig. 15). The self-equilibrium stress part components, $\tau_{x\theta}$ (Eq. 1) and τ_{tw} (Eq. 8) are assumed to be important for fatigue crack development at the considered notch location only and another τ_{se} contribution for the symmetry part will be ignored. The far field stress component is assumed to be dominant for $\{1/2 < (r/t_p) < 1\}$, meaning that no τ_{tw} correction is required for this region. For a pure out-of-plane shear force $F_{s,op}$ induced load case $(\tau_s = \tau_{ss})$, the notch stress formulation for $\rho = 0$ becomes:

$$\begin{aligned}\tau_{ns}\left(\frac{r}{t_p}\right) &= \tau_s f_{\rho=0}\left(\frac{r}{t_p}\right)\\ &= \tau_s\left[\left(\frac{r}{t_p}\right)^{\lambda_\tau-1}\mu_{\tau F}\cos(\lambda_\tau\beta) - \mu_{\tau M}\left\{2\left(\frac{r}{t_p}\right)-1\right\} - C_{tw}\left\{4\left(\frac{r}{t_p}\right)-1\right\}\right]\end{aligned} \tag{26}$$

and for $\rho > 0$:

$$\begin{aligned}\tau_{ns}\left(\frac{r}{t_p}\right) &= \tau_s f_{\rho>0}\left(\frac{r}{t_p}\right)\\ &= \tau_s\left[\left(\frac{r'}{t_p}\right)^{\lambda_\tau-1}\mu_{\tau F}\cos(\lambda_\tau\beta)\left\{1+\left(\frac{r_0}{t_p}\right)^{2\lambda_\tau}\left(\frac{r'}{t_p}\right)^{-2\lambda_\tau}\right\} - \mu_{\tau M}\left\{2\left(\frac{r'}{t_p}\right)-1\right\} - C_{tw}\left\{4\left(\frac{r'}{t_p}\right)-1\right\}\right].\end{aligned} \tag{27}$$

To calculate the coefficients $\mu_{\tau F}$ and $\mu_{\tau M}$, half the plate thickness is considered. Using force and moment equilibrium only is not sufficient and a symmetry condition has been added as 3rd equation. However, the system of equations has become over determined, meaning a least squares solution will be obtained. Allowing for some relaxation, i.e. ignoring moment equilibrium, provides quite accurate results – like for mode-I [9]. Force equilibrium in a weak form for $\rho = 0$:

$$\int_0^{1/2}\tau_n\left(\frac{r}{t_p}\right)\mathrm{d}\left(\frac{r}{t_p}\right) = \int_0^{1/2}\tau_s\,\mathrm{d}\left(\frac{r}{t_p}\right) \tag{28}$$

provides

$$\mu_{\tau F} = \frac{\lambda_\tau\left(C_{tw}+1\right)}{\cos\left(\lambda_\tau\beta\right)2^{1-\lambda_\tau}\left(1+\frac{\lambda_\tau}{2}\left(\lambda_\tau-1\right)\right)}. \tag{29}$$

In case $\rho > 0$, the coordinate system transformation (Eqs. 4 and 5) becomes involved and force equilibrium in weak form:

$$\int_{\left(\frac{r_0}{t_p}\right)}^{\left(\frac{2r_0+1}{2t_p}\right)}\tau_n\left(\frac{r}{t_p}\right)\mathrm{d}\left(\frac{r}{t_p}\right) = \int_0^{1/2}\tau_s\,\mathrm{d}\left(\frac{r}{t_p}\right) \tag{30}$$

denotes

$$\mu_{\tau F} = \frac{\begin{array}{l}\lambda_\tau\left\{\lambda_\tau\left(\frac{r_0}{t_p}\right)^{2\lambda_\tau}\left(\frac{2r_0+1}{2t_p}\right)\left(\frac{4r_0+1}{4t_p^2}\right)\left\{2^{\lambda_\tau-1}+C_{tw}2^{\lambda_\tau}\left(\frac{1}{2t_p}\right)\right\} - \right.\\ 2^{\lambda_\tau+1}C_{tw}\left[\left(\frac{2r_0+1}{2t_p}\right)^2\left(\frac{r_0}{t_p}\right)^{\lambda_\tau} - \left(\frac{2r_0+1}{2t_p}\right)\left(\frac{r_0}{t_p}\right)^{\lambda_\tau+1} - \left(\frac{2r_0+1}{2t_p}\right)^{2+\lambda_\tau} + \right.\\ \left.\left.\left(\frac{r_0}{t_p}\right)\left(\frac{2r_0+1}{2t_p}\right)^{\lambda_\tau+1}\right] - 2^{\lambda_\tau}\left[\left(\frac{r_0}{t_p}\right)^{\lambda_\tau}\left(\frac{2r_0+1}{2t_p}\right) - \left(\frac{2r_0+1}{2t_p}\right)^{\lambda+1}\right]\right\}\end{array}}{\begin{array}{l}\cos\left(\lambda_\tau\theta\right)\left(\frac{2r_0+1}{2t_p}\right)\left[\lambda_\tau\left[\left(\frac{4r_0+1}{4t_p^2}\right)\right]\left(\frac{r_0}{t_p}\right)^{2\lambda_\tau} - 2\left(\frac{r_0}{t_p}\right)^{\lambda_\tau} + \right.\\ \left.2\left(\frac{2r_0+1}{2t_p}\right)^{\lambda_\tau}\right]\left\{\left(\frac{2r_0+1}{2t_p}\right)\lambda_\tau 2^{\lambda_\tau}\left[\left(\frac{1}{2t_p}\right)\right]\left(\frac{r_0}{t_p}\right)^{2\lambda_\tau} + \right.\\ \left.2^{\lambda_\tau}\left[\left(\frac{2r_0+1}{2t_p}\right)^{\lambda_\tau} - \left(\frac{r_0}{t_p}\right)^{\lambda_\tau}\right] + \frac{\lambda_\tau(\lambda_\tau-1)}{2t_p^2}\right\}\end{array}}. \tag{31}$$

Imposing symmetry:

$$\left.\frac{\mathrm{d}\tau_n\left(\frac{r}{t_p}\right)}{\mathrm{d}\left(\frac{r}{t_p}\right)}\right|_{\left(\frac{r}{t_p}=\frac{1}{2}\right)} = 0 \tag{32}$$

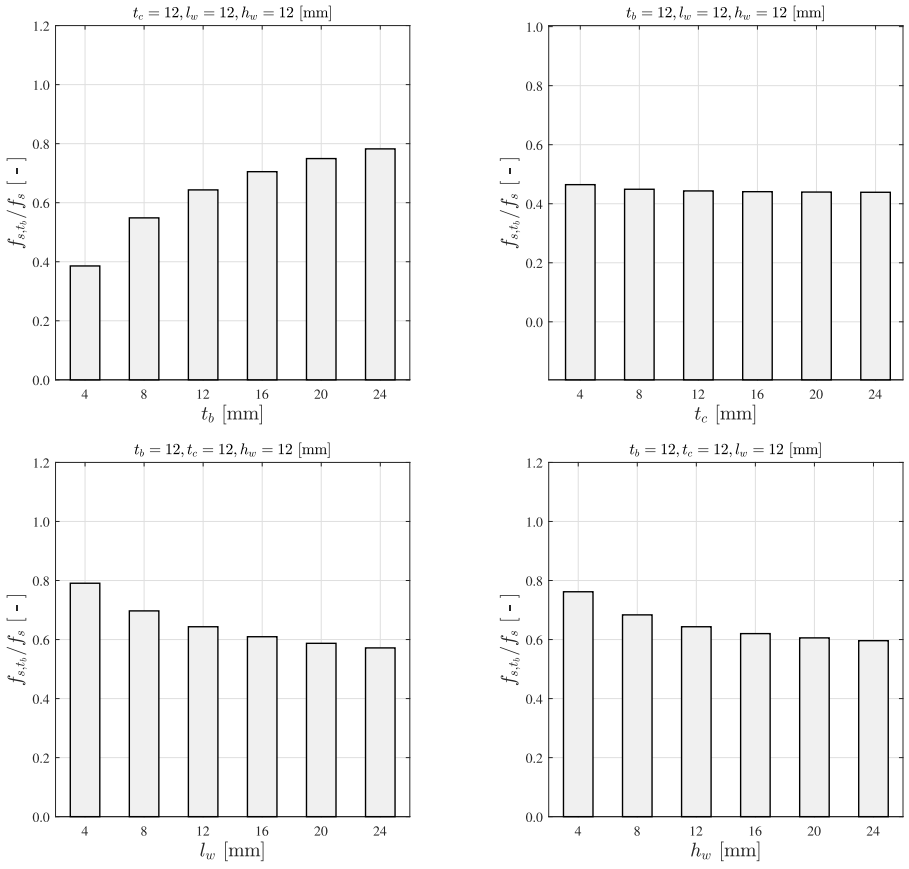

Fig. 9. Relative base plate shear load for a DS welded T-joint, varying t_b, t_c, l_w and h_w for $R_t \to \infty$.

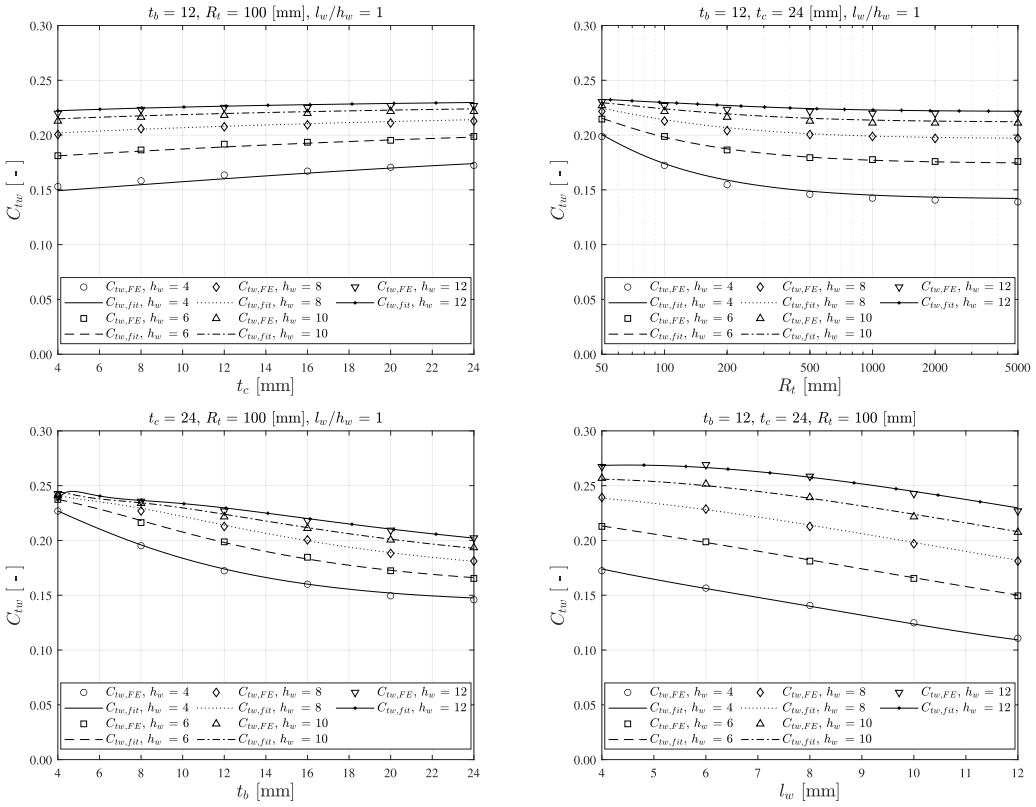

Fig. 10. Required C_{tw} value and fit estimate for a DS welded T-joint varying t_b, t_c, l_w, h_w and R_t.

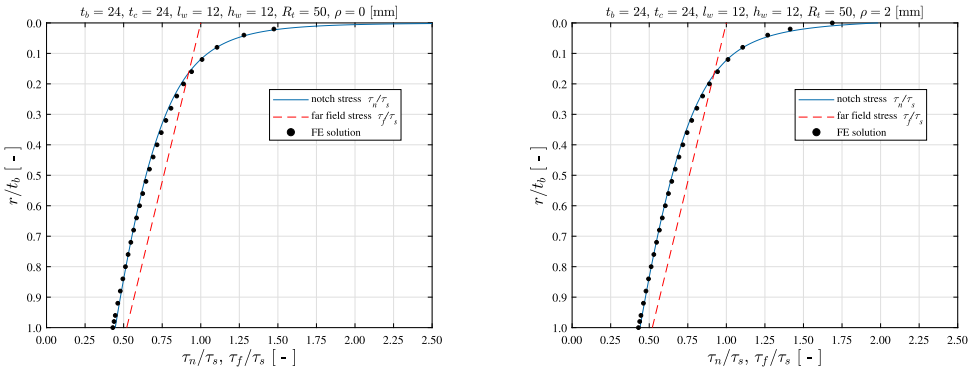

Fig. 11. Weld toe notch stress distribution for $\rho = 0$ (left) and $\rho > 0$ (right) for a DS welded T-joint; $r_{\tau_s} = 0.24$.

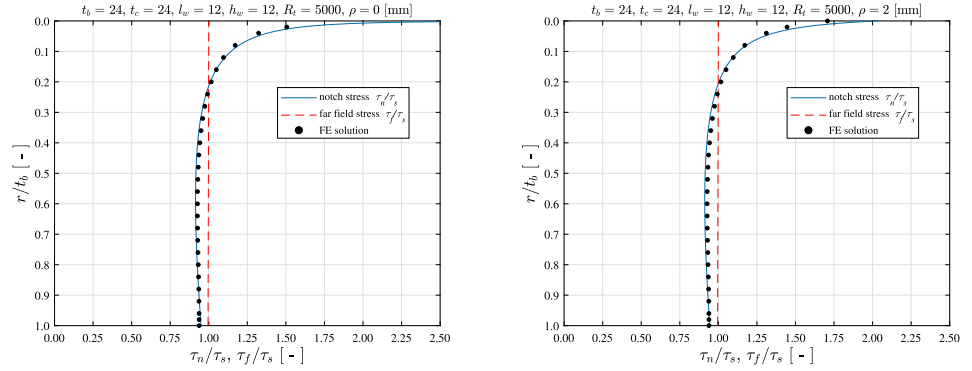

Fig. 12. Weld toe notch stress distribution for $\rho = 0$ (left) and $\rho > 0$ (right) for a DS welded T-joint; $r_{\tau_s} = 0$.

yields $\mu_{\tau M} = (2\lambda_\tau(\lambda_\tau - 1) - 4C_{tw})(\lambda_\tau^2 - \lambda_\tau + 2)^{-1}$ for $\rho = 0$. However, like observed for moment equilibrium in case of non-symmetry (Section 2.4), substitution in $\tau_n(r/t_p)$ provides a C_{tw} independent equation, since the introduced anti-symmetric term and the weld load carrying stress have the same form. Ignoring the weld load carrying stress contribution yields for $\rho = 0$:

$$\mu_{\tau M} = \frac{2\lambda_\tau(\lambda_\tau - 1)}{\lambda_\tau^2 - \lambda_\tau + 2} \tag{33}$$

and for $\rho > 0$, considering the notch radius induced shift of the coordinate system origin (Eqs. 4 and 5):

$$\mu_{\tau M} = \frac{\left(\frac{2r_0+1}{2t_p}\right)^2 \lambda_\tau \left\{ 2^{\lambda_\tau}\left(\frac{r_0}{t_p}\right)^{2\lambda_\tau} + 4(\lambda_\tau - 1)\right\}}{\left\{ \lambda_\tau 2^{\lambda_\tau}\left(\frac{r_0}{t_p}\right)^{2\lambda_\tau}\left(\frac{2r_0+1}{4t_p^2}\right) + 2^{\lambda_\tau}\left[\left(\frac{2r_0+1}{2t_p}\right)^{\lambda_\tau} - \left(\frac{r_0}{t_p}\right)^{\lambda_\tau}\right] + \frac{\lambda_\tau(\lambda_\tau-1)}{2t_p^2}\right\}}. \tag{34}$$

In order to acquire the pure torsion moment M_t induced notch stress distribution in a similar formulation as for non-symmetry (Eq. 15), i.e. including a far field torsion stress projection, $\tau_{ns}(r/t_p)$ needs to be shifted first by $\{1 - f(r/t_p = 1/2)\}$ – with $f(r/t_p) = f_{\rho=0}(r/t_p)$ or $f(r/t_p) = f_{\rho>0}(r/t_p)$ for respectively $\rho = 0$ and $\rho > 0$ – in order to meet the condition $\tau_{nt}(r/t_p = 1/2) = 0$. To satisfy anti-symmetry, the τ_{nt} gradient at $(r/t_p = 1/2)$ should be equal to the far field torsion value -2. Subtracting the shift in terms of a torsion stress gradient $-2\{1 - f(r/t_p = 1/2)\}$ from the unit stress 1, the obtained formulation needs to be scaled using $\{2f(r/t_p = 1/2) - 1\}$ and becomes for $\rho = 0$:

$$\tau_{nt}\left(\frac{r}{t_p}\right) = \tau_s\left[2f_{\rho=0}\left(\frac{r}{t_p} = \frac{1}{2}\right) - 1\right]\left\{ f_{\rho=0}\left(\frac{r}{t_p}\right) + \left[1 - f_{\rho=0}\left(\frac{r}{t_p} = \frac{1}{2}\right)\right] - 2\left(\frac{r}{t_p}\right)\right\} \tag{35}$$

with

$$f_{\rho=0}\left(\frac{r}{t_p} = \frac{1}{2}\right) = \left[\left(\frac{1}{2}\right)^{\lambda_\tau - 1}\mu_{\tau F}\cos(\lambda_\tau\beta) - C_{tw}\right] \tag{36}$$

and for $\rho > 0$:

$$\tau_{nt}\left(\frac{r'}{t_p}\right) = \tau_s\left[2f_{\rho>0}\left(\frac{r'}{t_p} = \frac{1}{2}\right) - 1\right]\left\{ f_{\rho>0}\left(\frac{r'}{t_p}\right) + \left[1 - f_{\rho>0}\left(\frac{r'}{t_p} = \frac{1}{2}\right)\right] - 2\left(\frac{r'}{t_p}\right)\right\} \tag{37}$$

with

$$f_{\rho>0}\left(\frac{r'}{t_p} = \frac{1}{2}\right) = \left[\left(\frac{2r_0+1}{2t_p}\right)^{\lambda_\tau - 1}\mu_{\tau F}\cos(\lambda_\tau\beta)\cdot \left\{1 + \left(\frac{r_0}{t_p}\right)^{2\lambda_\tau}\left(\frac{2r_0+1}{2t_p}\right)^{-2\lambda_\tau}\right\} - \mu_{\tau M}\left\{2\left(\frac{2r_0+1}{2t_p}\right) - 1\right\} - C_{tw}\left\{4\left(\frac{2r_0+1}{2t_p}\right) - 1\right\}\right]. \tag{38}$$

Finally, adopting a linear superposition principle, the mode-III stress distribution for symmetry can be obtained for $\rho = 0$ using the τ_{ns} and τ_{nt} formulations (Eqs. 26 and 35) as well as structural stress relations

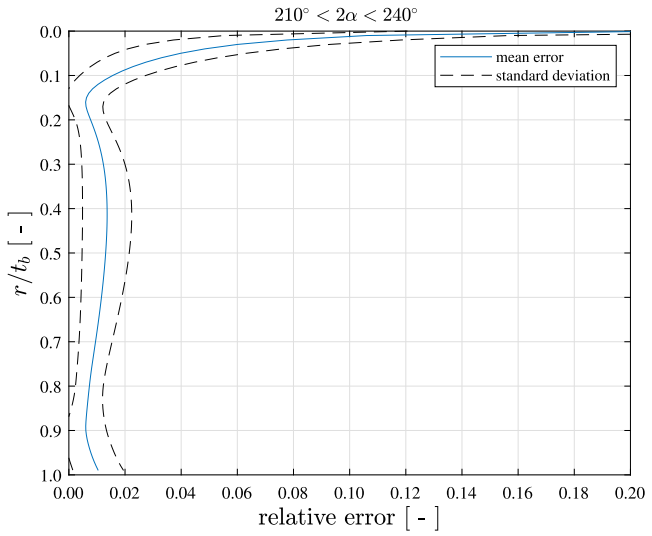

Fig. 13. Relative stress distribution error for DS welded T-joint, comparing the FE solutions and the analytical results. The fillet weld angle is in between 30 and 60 [deg], i.e $210° < 2\alpha < 240°$.

(Eq. 13):

$$\tau_n\left(\frac{r}{t_p}\right) = \tau_s\left(\left[1-2r_{\tau_s}\left\{1-f_{\rho=0}\left(\frac{r}{t_p}=\frac{1}{2}\right)\right\}\right]f_{\rho=0}\left(\frac{r}{t_p}\right)+\left[2f_{\rho=0}\left(\frac{r}{t_p}=\frac{1}{2}\right)-1\right]\left\{\left[1-f_{\rho=0}\left(\frac{r}{t_p}=\frac{1}{2}\right)\right]-2\left(\frac{r}{t_p}\right)\right\}\right). \quad (39)$$

The same formulation applies for $\rho > 0$, using $f_{\rho>0}(r/t_p = 1/2)$ rather than $f_{\rho=0}(r/t_p = 1/2)$; i.e. (Eq. 27) and (Eq. 37). Like for non-symmetry (Section 2.4), the $\rho = 0$ expressions are a $\rho > 0$ limit case. For a tubular structure with attachment involving a DS welded cruciform joint and exposed to a torsion moment M_t (Fig. 15), the structural stress ratio r_{τ_s} changes for varying tube radius R_t. For the limit cases, respectively $R_t \to t_b$ (corresponding to a solid shaft) and $R_t \to \infty$ (corresponding to a quasi-planar structure), the pure torsion and pure shear case appear, meaning that for symmetry – in contrast to non-symmetry (Section 2.4) – both extremes can be considered to establish the r_{τ_s} dependent weld load carrying stress $\tau_s C_{tw}$ behaviour.

Investigating the relative load path contributions for the DS welded cruciform joint, three parallel load paths are involved: one through the base plate and two through the weld and cross plate. The shear forces through the base plate (Fig. 16; $R_t \to \infty$) are relatively small in comparison to the DS welded T-joint values (Fig. 9) because of the smaller stiffness contribution of each load path. The trends for f_s (Fig. 9 for the T-joint – as well as Fig. 16; $R_t \to \infty$ for the cruciform joint) and m_t (Fig. 16; $R_t \to t_b$) are the same. For m_t, the radius dependent torsion stiffness is involved for all load paths and becomes larger towards the outer load path through the weld and cross plate, clarifying the relatively small $(m_{t,t_b}/m_t)$ values. For increasing t_b, the shear force and torsion moment through the base plate increase because of increasing base plate load path stiffness. The weld and cross plate load path torsion stiffness increases for increasing t_c, l_w, and h_w, meaning the base plate load path contribution decreases. Like for non-symmetry (Section 2.4), a 4th order polynomial fitting function (Eq. B.2) has been established to capture C_{tw} estimates. The weld load carrying stress turns out to be virtually ρ independent for realistic values: $(\rho/t_b) \leq 0.2$ and has been neglected in establishing the C_{tw} fitting function.

For DS welded cruciform joints, the weld load carrying stress level does not even reach 5 [%] of τ_s (Fig. 17). Since $R_t = 100$ [mm], the far field stress involves both a (constant) shear force and (linear) torsion moment induced contribution. For varying t_c and l_w, the trends (Fig. 17) are the same and opposite to the relative base plate loads (Fig. 16) as expected because of the same physics. Although, a decreasing C_{tw} might be expected for increasing t_b and h_w (Fig. 16), the increased radius dependent torsion stiffness for the outer load path through the weld and cross plate is responsible for counteracting behaviour and provides even a small C_{tw} increase. Like for the non-symmetry case (Section 2.4), asymptotically decreasing C_{tw} behaviour – related to the pure shear limit case ($r_{\tau_s} = 0$) – can be observed for increasing R_t, meaning C_{tw} is relatively small in comparison to the pure torsion case ($r_{\tau_s} = 1$).

Monotonic through-thickness stress distributions at the weld toe notch of the base plate are shown (Figs. 18 and 19) for a pure torsion moment ($r_{\tau_s} = 1$) and combined load case ($r_{\tau_s} = 0.24$); the torsion moment is applied counter-clockwise. A non-monotonic one is shown (Fig. 20) for a pure shear force ($r_{\tau_s} = 0$). For $\{0 \leq (r/t_b) \leq (1/2)\}$ equilibrium conditions are (approximately) satisfied as imposed. The (anti-)symmetry condition (Eq. 32) ensures a stress gradient close to r_{τ_s} for $\{(1/2) \leq (r/t_b) \leq 1\}$. Converged solid FE model solutions are added for comparison, showing that the semi-analytical $\tau_n(r/t_p)$ formulations (Eq. 39) provide accurate weld notch stress distributions. Like for the non-symmetry case (Section 2.4), three zones can be identified meaning stress field similarity is maintained. In general, the relative

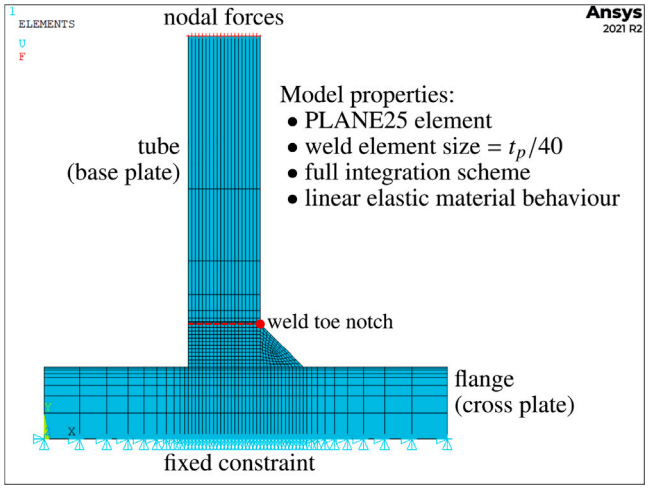

Fig. 14. Two-dimensional harmonic axisymmetric FE model for a non-symmetric T-joint.

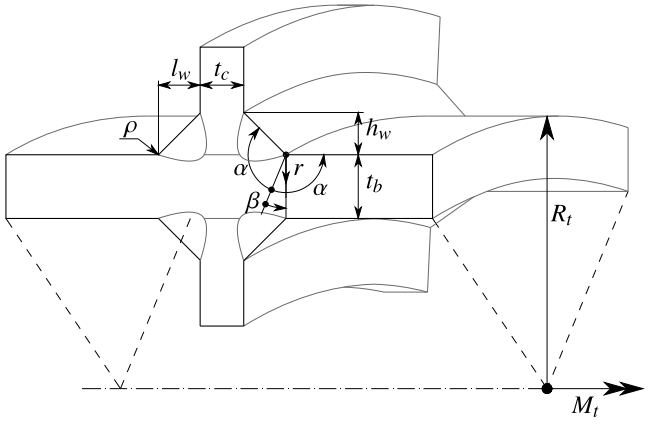

Fig. 15. DS welded cruciform joint showing symmetry with respect to $(t_b/2)$, either in a tubular or planar ($R_t \to \infty$) structure.

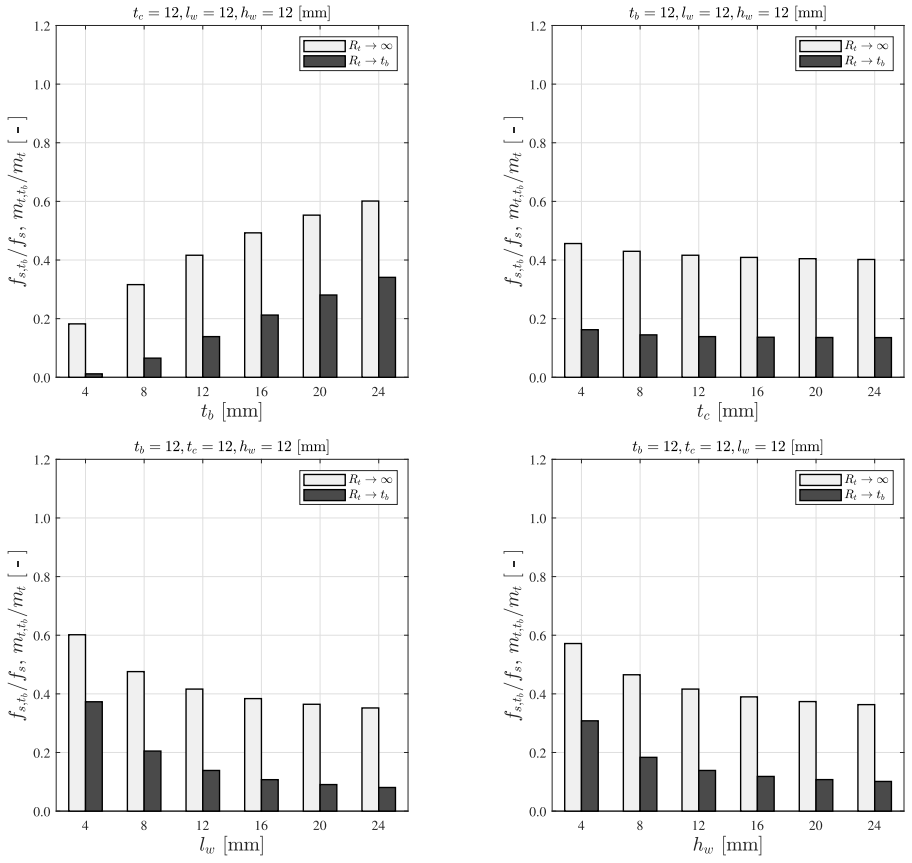

Fig. 16. Relative base plate shear load for a DS welded cruciform joint, varying t_b, t_c, l_w and h_w for both $R_t \to \infty$ and $R_t \to t_b$.

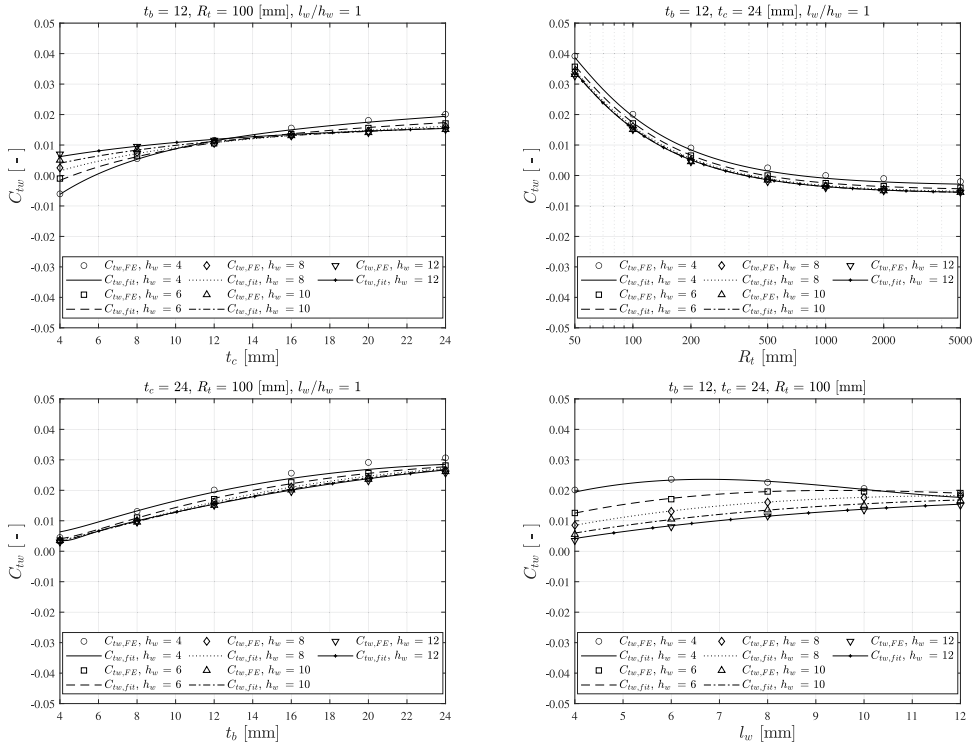

Fig. 17. Required C_{tw} value and fit estimate for a DS welded cruciform joint, varying t_b, t_c, l_w, h_w and R_t.

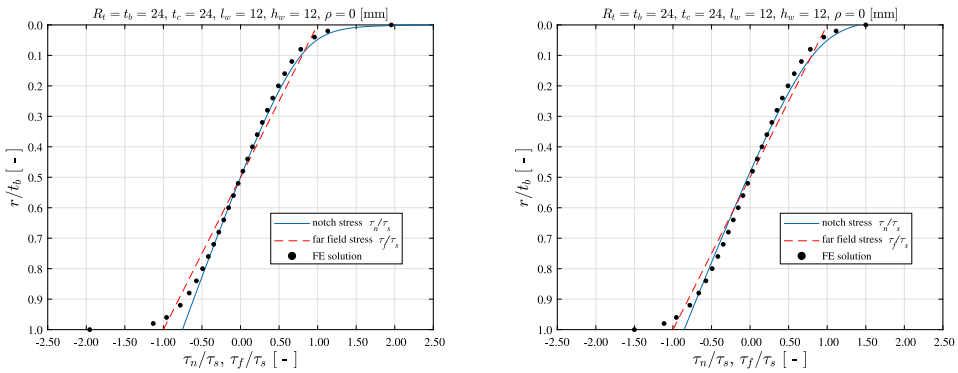

Fig. 18. Weld toe notch stress distribution for $\rho = 0$ (left) and $\rho > 0$ (right) for a DS welded cruciform joint; $r_{\tau_s} = 1$.

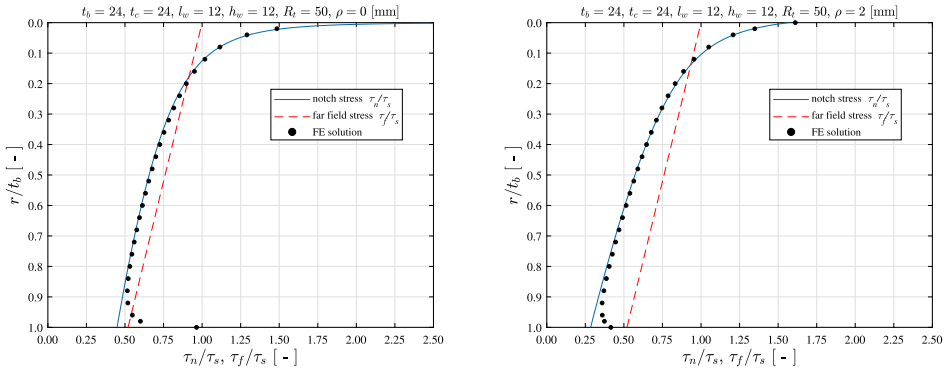

Fig. 19. Weld toe notch stress distribution for $\rho = 0$ (left) and $\rho > 0$ (right) for a DS welded cruciform joint; $r_{\tau_s} = 0.24$.

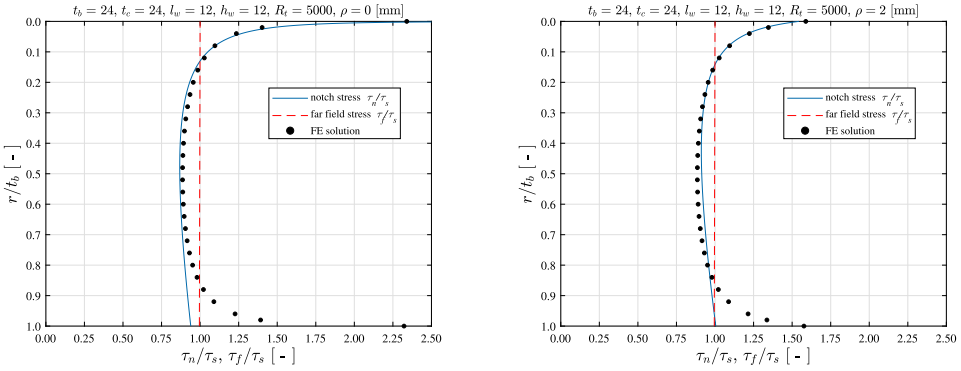

Fig. 20. Weld toe notch stress distribution for $\rho = 0$ (left) and $\rho > 0$ (right) for a DS welded cruciform joint; $r_{\tau_s} = 0$.

error (Fig. 21) – obtained considering all stress distributions for the full parameter range – is within 5 [%] for $\{0 \leq (r/t_b) \leq (1/2)\}$. Relatively large errors appear in the far field dominated stress gradient zone since the notch contribution for the symmetry part in $\{(1/2) \leq (r/t_b) \leq 1\}$ has been neglected.

3. Mode-III welded joint fatigue resistance

Using fatigue resistance data from literature (Section 3.1), the mode-III welded joint mid-cycle fatigue resistance characteristics will be established using the nominal stress concept (Section 3.2), as well as the effective notch stress concept (Section 3.3) employing the semi-analytical weld notch stress formulations (Section 2).

3.1. Fatigue resistance data

Principally, only data series involving steel specimens with circular cross-sections – typical tubular structural joints – are considered (Fig. 22 and Table 1), in order to ensure pure mode-III response conditions at the governing fatigue sensitive location; a DS welded T-joint geometry showing non-symmetry with respect to $(t_p/2)$ of the hot spot type C [8,9]. Only specimens showing weld toe induced fatigue damage are included, involving predominantly failures and some run-outs. The sample size is ~50.

The external loading basically involves a torsion moment M_t. For gripping and/or load application purposes, the specimens typically contain flanges. In case of non-circular cross-sections, warping constrains will introduce a mode-I response contribution at the governing hot spot, explaining why the often used square cross-section data [38,39] is not included this time. Specimens involving attachments [40] are not included as well. Although the external loading involves a torsion moment M_t, the attachment locally affects the stiffness distribution and the governing hot spot – type A – response involves a mode-I contribution.

The loading & response ratio $R = -1$ for most data series, meaning the loading & response condition is fully reversed and the mean

Table 1
Fatigue resistance data from literature.

Author	t_b [mm]	t_c [mm]	l_w [mm]	h_w [mm]	R_i [mm]	ρ [mm]	R	No. specimens	Thermal condition
Sonsino [32]	10.0	25.0	9.0	9.0	44.45	0.45	−1	4	stress-relieved
Yousefi [33]	8.0	25.0	10.0	10.0	42.42	n.a.	[0; −1]	[9; 8]	stress-relieved
Siljander [34]	9.5	9.5	8.0	8.0	25.40	0.18	[0; −1]	[2; 6]	stress-relieved
Witt [35]	8.0	16.0	9.0	9.0	44.45	n.a.	−1	11	stress-relieved
Seeger [36]	8.0	20.0	6.3	6.3	54.00	1.00	−1	6	stress-relieved
Yung [37]	8.0	8.0	7.7	7.7	23.80	n.a.	−1	2	as-welded

component is zero. For some data series $R = 0$, reflecting a repeated (impact) loading & response condition with non-zero mean. Since the thermal condition for the majority of the specimens is stress-relieved and for some as-welded – introducing a welding induced mean component as well, the influence of mean stress will be investigated. Looking at the life time range of the considered data, $N = (10^4 \sim 5.10^6)$ cycles, meaning virtually all data reflects mid-cycle fatigue characteristics. Correlating a fatigue strength criterion S to the fatigue life time N, typically a (n approximately) log–log linear dependency is observed

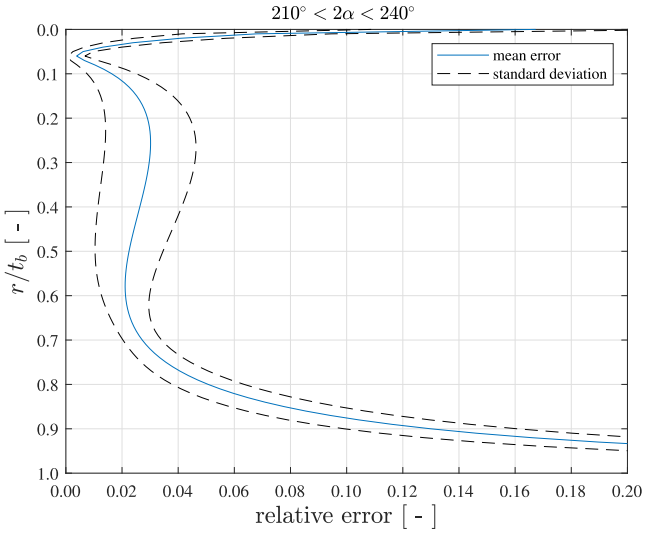

Fig. 21. Relative stress distribution error for DS welded cruciform joint, comparing the FE solutions and the analytical results. The fillet weld angle is in between 30 and 60 [deg], i.e $210° < 2\alpha < 240°$.

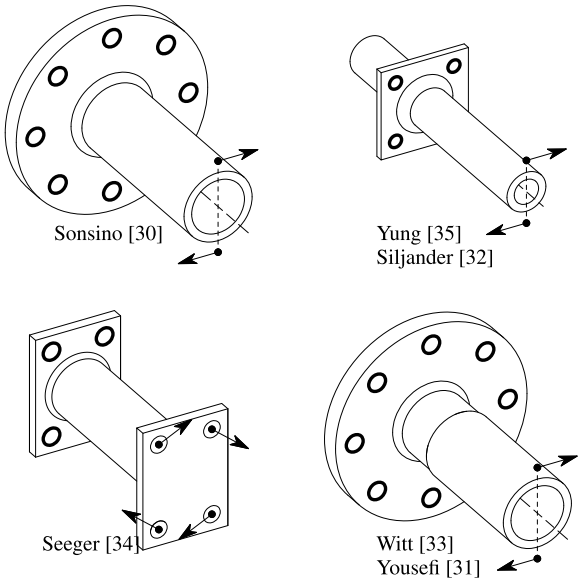

Fig. 22. Fatigue test specimen geometry, external loading (arrows) and constraints (thick lines).

and a Basquin type of relation is naturally adopted [7]: $\log(N) = \log(C) - m\log(S)$. One way to estimate the single slope curve parameters, intercept $\log(C)$ and slope m as respectively the endurance and damage mechanism coefficient, is using linear regression on fatigue life time: $\log(N) = \log(C) - m\log(S) + \sigma\epsilon$, introducing the scatter (i.e. performance) parameter σ. The maximum likelihood approach [9,41] will be employed to obtain the most likely parameter vector estimate $\hat{\boldsymbol{\Phi}}$: $\max_{\boldsymbol{\Phi}} \{\mathcal{L}(\boldsymbol{\Phi}; N|S)\}$ with $\boldsymbol{\Phi} = \{\log(C), m, \sigma\}$.

3.2. Nominal stress assessment

For reference purposes, the nominal stress criterion $S_n = \Delta\tau_{nom}$, a global structural detail- and linear elastic intact geometry parameter [2], will be used to establish the mid-cycle fatigue resistance characteristics. The intercept $\log(C)$ defines the fatigue strength and is typically expressed in terms of FATigue classes and detail CATegories. The damage mechanism is assumed to be similar for all structural details, meaning the slope m is invariant. As long as material, geometry, loading & response, environment as well as failure location and weld quality fit the FAT or CAT description, computational effort is limited and concept complexity is relatively low. However, local geometry and loading & response variations are not explicitly considered, paying off in terms of fatigue resistance accuracy since S_n is processed as point criterion, as 'local' nominal stress, meaning (notch stress gradient induced) size effects are not taken into account explicitly and have to be corrected for. Although a spatial description of a loading & response cycle requires two parameters, e.g. range and ratio $R = (M_{t,\min}/M_{t,\max}) = (\tau_{\min}/\tau_{\max})$, the ratio – reflecting a mean stress effect – is typically not explicitly considered. However, Walker's mean stress model will be adopted, typically providing the best results for welded joints [7,8,42] and turning the nominal stress criterion into an effective one:

$$S_{n,\text{eff}} = \Delta\tau_{n,\text{eff}} = \frac{\Delta\tau_{nom}}{(1-R)^{1-\gamma}} \quad \forall\ 0 \le \gamma \le 1. \tag{40}$$

For $\gamma \to 1$, the nominal stress range $\Delta\tau_{nom}$ dominates the fatigue resistance; the mean stress becomes governing for $\gamma \to 0$. The loading & response ratio coefficient γ is a fitting parameter and will be added to the parameter vector: $\boldsymbol{\Phi}\{\log(C), m, \gamma, \sigma\}$. Assuming that the fatigue life time N is most likely log(Normal) distributed, maximum likelihood based regression analysis of the mode-III welded joint fatigue resistance data confirms the log–log linear behaviour (Fig. 23). The parameter confidence is relatively large (Table 2), and in agreement with expectations considering the sample size (Section 3.1).

The fatigue strength as reflected in $\log(\hat{C})$ is for the R95C75 design curve – reliability level is 95 [%] and confidence level is 75 [%] – at $N = 2 \cdot 10^6$ cycles $\sim$ 150 [MPa], meaning that the IIW FAT80 [16] and Eurocode CAT80 [17] seem conservative. Slope $\hat{m} \sim 4.7$ is close to the typical design value $m = 5$ [16,17]. The standard deviation $\hat{\sigma} \sim 0.29$ can be used to calculate the strength scatter band index $T_{\sigma S_n} = 1 : (S_{n,10}/S_{n,90}) = 1 : 1.25$, the fatigue strength ratio for 10 [%] and 90 [%] probability of survival, and turns out to be already small in comparison to a typical value of 1:1.5 [12].

Walker's loading & response ratio coefficient $\hat{\gamma} \sim 1$, meaning that the mean stress does not affect the mode-III fatigue resistance, in contrast to mode-I [7,8]. The external loading induced mean shear stress contribution for the considered data sets with $R = \{0, -1\}$

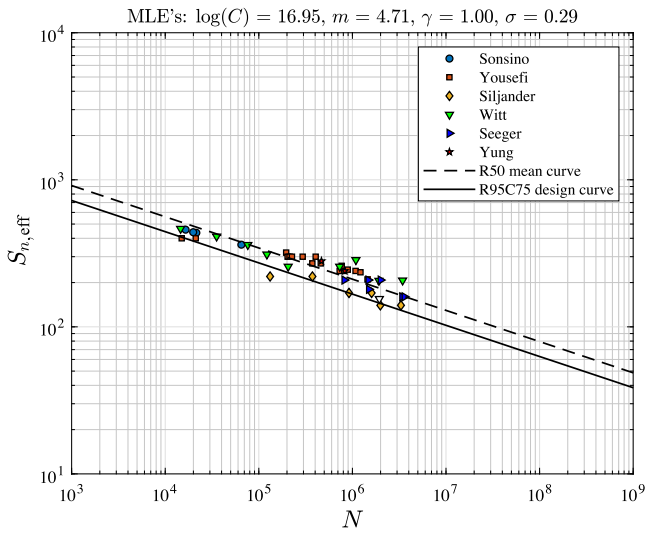

Fig. 23. Nominal stress based fatigue resistance including mean stress correction.

Table 2
Nominal stress based parameter estimates and 75 [%] lower and upper confidence bounds.

Parameter		
log(C)	16.95	[16.06, 17.85]
m	4.71	[4.34, 5.08]
ρ^*	/	/
γ	1.00	[0.97, 1.00]
σ	0.29	[0.26, 0.33]

is insignificant and at the same time the contribution of the quasi-constant welding induced residual stress seems negligible as well, since the stress-relieved and as-welded data match the same scatter band. Whether the welding induced residual stress would be a mode-I or mode-III component – or even a mixed one – is unknown, although the mode-I component effect is typically small in the mid-cycle fatigue region as well [43], but can become more significant when shifting to the high-cycle fatigue region [1]. The statement that stress-relieve clearly influences mode-III fatigue resistance [39] seems to be a result of a comparison to a mode-I fatigue resistance curve. Different mean stress effects have been reported for various materials and geometries – both plane and notched [44–48]. However, common denominator seems that for mode-III mean stress effects are less significant than for mode-I, at least in case more ductile materials like steel are involved. Since $\gamma \sim 0.9$ for mode-I [7], the same observation applies to the fatigue resistance of welded joints in steel (maritime) structures.

3.3. Effective notch stress assessment

Although for welded joints (short and long) crack growth dominates the damage process, the fatigue life time N is predominantly spent in the notch affected region [6], meaning a local notch characteristic intact geometry parameter rather than a cracked geometry one can be adopted as fatigue strength criterion as well. Since the (as) weld(ed) notch radius ρ is typically small, a zone 1 peak stress criterion would be too conservative. Adopting a micro- and meso-structural notch support hypothesis, an effective notch stress estimate τ_e can be obtained by averaging the notch stress distribution along the expected crack path over a material characteristic micro- and meso-structural length ρ^*, partially incorporating a zone 2 notch stress gradient – and zone 3 far field stress gradient contribution as well [7,8,10–13,49]:

$$\tau_e = \frac{t_p}{\rho^*} \int_0^{\frac{\rho^*}{t_p}} \tau_n\left(\frac{r}{t_p}\right) \mathrm{d}\left(\frac{r}{t_p}\right). \tag{41}$$

Typically, a solid FE model solution is required in order to estimate τ_e. However, taking advantage of the stress distribution formulations (Eqs. 14, 15 and 39), the effective notch stress criterion $S_e = \Delta\sigma_e$ in case of non-symmetry becomes for $\rho = 0$:

$$S_e = \frac{\Delta\tau_s}{\lambda_\tau}\frac{t_p}{\rho^*}\left\{\cos(\lambda_\tau\beta)\mu_{\tau F}\left(\frac{\rho^*}{t_p}\right)^{\lambda_\tau} - \lambda_\tau\left(\frac{\rho^*}{t_p}\right)\left[\left(\frac{\rho^*}{t_p}\right)(\mu_{\tau M} + r_{\tau_s} + C_{tw}) - \mu_{\tau M} - C_{tw}\right]\right\} \tag{42}$$

and for $\rho > 0$:

$$\begin{aligned} S_e = {} & \frac{\Delta\tau_s}{\lambda_\tau}\left(\frac{r_0+\rho^*}{t_p}\right)^{-1} \cdot \\ & \left\{\cos(\lambda_\tau\beta)\mu_{\tau F}\left[\left(\frac{r_0+\rho^*}{t_p}\right)^{\lambda_\tau} - \left(\frac{r_0}{t_p}\right)^{\lambda_\tau}\right] - \right. \\ & \cos(\lambda_\tau\beta)\left(\frac{r_0}{t_p}\right)^{2\lambda_\tau}\mu_{\tau F}\left[\left(\frac{r_0+\rho^*}{t_p}\right)^{-\lambda_\tau} - \left(\frac{r_0}{t_p}\right)^{-\lambda_\tau}\right] - \\ & \left.\lambda_\tau\frac{\rho^*}{t_p}\left[\left(\frac{2r_0+\rho^*}{t_p}\right)\left(\mu_{\tau M} + r_{\tau_s} + C_{tw}\right) - \mu_{\tau M} - C_{tw}\right]\right\}. \end{aligned} \tag{43}$$

In case of symmetry with respect to $(t_p/2)$ and $\rho = 0$:

$$\begin{aligned} S_e = {} & \frac{2\Delta\tau_s}{\lambda_\tau}\frac{t_p}{\rho^*}\left\{\cos(\lambda_\tau\beta)\mu_{\tau F}\left(\frac{\rho^*}{t_p}\right)^{\lambda_\tau}\left\{\frac{1}{2} + r_{\tau_s}\left[f_{\rho=0}\left(\frac{r}{t_p}=\frac{1}{2}\right) - 1\right]\right\} - \right. \\ & \lambda_\tau\left(\frac{\rho^*}{t_p}\right)\left[\left(\frac{\rho^*}{t_p}\right)\left\{\frac{\mu_{\tau M}}{2} + f_{\rho=0}\left(\frac{r}{t_p}=\frac{1}{2}\right) + C_{tw} - \frac{1}{2} + \right.\right. \\ & \left.\left[f_{\rho=0}\left(\frac{r}{t_p}=\frac{1}{2}\right) - 1\right](\mu_{\tau M} + 2C_{tw})\, r_{\tau_s}\right\} - \\ & \left[f_{\rho=0}\left(\frac{r}{t_p}=\frac{1}{2}\right) - 1\right](\mu_{\tau M} + C_{tw})\, r_{\tau_s} + \left[f_{\rho=0}\left(\frac{r}{t_p}=\frac{1}{2}\right)\right]^2 - \\ & \left.\left.\frac{1}{2}\left[\mu_{\tau M} + 3f_{\rho=0}\left(\frac{r}{t_p}=\frac{1}{2}\right) + C_{tw} - 1\right]\right]\right\} \end{aligned} \tag{44}$$

and for $\rho > 0$:

$$\begin{aligned} S_e = {} & \frac{2\Delta\tau_s}{\lambda_\tau}\left(\frac{r_0+\rho^*}{t_p}\right)^{-1} \cdot \\ & \left\langle\left[\cos(\lambda_\tau\beta)\mu_{\tau F}\left\{\frac{1}{2} + \left[f_{\rho>0}\left(\frac{r}{t_p}=\frac{1}{2}\right) - 1\right]r_{\tau_s}\right\}\right]\cdot \right. \\ & \left\{\left(\frac{r_0}{t_p}\right)^{2\lambda_\tau}\left[\left(\frac{r_0}{t_p}\right)^{-\lambda_\tau} - \left(\frac{r_0+\rho^*}{t_p}\right)^{-\lambda_\tau}\right] - \right. \\ & \left.\left[\left(\frac{r_0}{t_p}\right)^{\lambda_\tau} - \left(\frac{r_0+\rho^*}{t_p}\right)^{\lambda_\tau}\right]\right\} - \\ & \lambda_\tau\frac{\rho^*}{t_p}\left\{r_{\tau_s}\left[f_{\rho>0}\left(\frac{r}{t_p}=\frac{1}{2}\right) - 1\right]\cdot\right. \\ & \left[(\mu_{\tau M} + 2C_{tw})\left(\frac{2r_0+\rho^*}{t_p}\right) - \mu_{\tau M} - C_{tw}\right] + \\ & \frac{\rho^*}{t_p}\left[\frac{\mu_{\tau M}}{2} + C_{tw} + f_{\rho>0}\left(\frac{r}{t_p}=\frac{1}{2}\right) - \frac{1}{2}\right] + \\ & \left[f_{\rho>0}\left(\frac{r}{t_p}=\frac{1}{2}\right)\right]^2 + \left[\left(\frac{r_0}{t_p}\right) - \frac{3}{2}\right]f_{\rho>0}\left(\frac{r}{t_p}=\frac{1}{2}\right) + \\ & \left.\left.\left(\frac{\mu_{\tau M}}{2} + C_{tw} - \frac{1}{2}\right)\left(\frac{r_0}{t_p}\right) + \frac{1}{2} - \frac{\mu_{\tau M}}{2} - \frac{C_{tw}}{2}\right\}\right\rangle. \end{aligned} \tag{45}$$

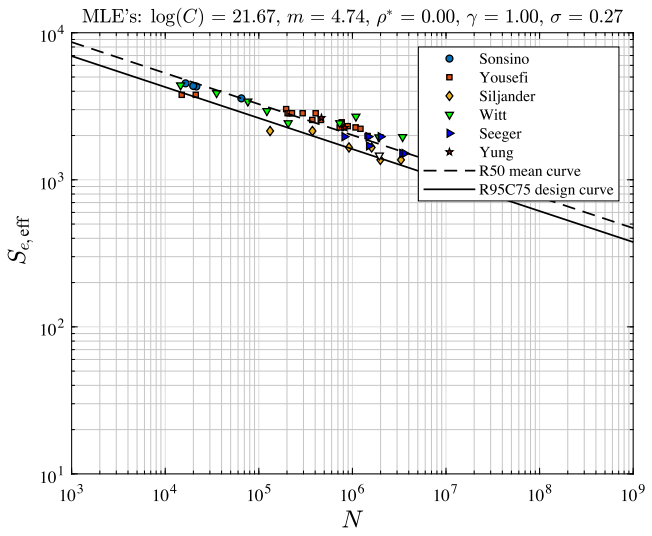

Fig. 24. Effective notch stress based fatigue resistance including mean stress correction for $\rho = 0$.

Table 3
Effective notch stress based parameter estimates and 75 [%] lower and upper parameter confidence bounds.

Parameter	$\rho = 0$		$\rho > 0$	
$\log(C)$	21.67	[20.25, 23.10]	18.80	[18.06, 19.53]
m	4.74	[4.40, 5.09]	5.08	[4.79, 5.35]
ρ^*	0.00	[0.00, 0.13]	0.12	[0.06, 0.21]
γ	1.00	[0.97, 1.00]	1.00	[0.98, 1.00]
σ	0.27	[0.24, 0.31]	0.21	[0.19, 0.24]

Table 4
$S_e - N$ normalised co-variance matrix for $\rho = 0$.

Parameter	$\log(C)$	m	ρ^*	γ	σ
$\log(C)$	1.00	−0.47	−0.33	0.35	−0.56
m		1.00	0.79	−0.61	0.79
ρ^*			1.00	0.00	0.33
γ				1.00	−0.83
σ					1.00

Incorporating Walker's mean stress model turns the notch stress criterion into an effective one:

$$S_{e,\text{eff}} = \frac{S_e}{(1-R)^{1-\gamma}}. \tag{46}$$

In order to obtain a most likely material characteristic length ρ^* and loading & response ratio coefficient γ estimate, both parameters will be added to the parameter vector $\Phi(\log C, m, \gamma, \rho^*, \sigma)$.

Adopting the Basquin type of relation (Section 3.1), maximum likelihood based regression analysis of the fatigue resistance data confirms the log–log linear behaviour (Fig. 24 and Table 3). Results are obtained for a most likely log(Normal) distributed fatigue life time N. Since ρ is typically a stochastic variable along the weld seam and quite small, $\rho = 0$ has been assumed.

Obviously, the fatigue strength parameter $\log(\widehat{C})$ is different from the nominal stress concept value (Section 3.2), since local information is included. As can be expected for log–log linear mid-cycle fatigue behaviour, the scaled co-variance matrix (Table 4) shows a highly correlated intercept $\log(C)$ and slope m. However, the introduced $\log(C) - \rho^*$ correlation seems responsible for the decreased parameter confidence. In comparison to the nominal stress value, slope m has hardly changed. The most likely material characteristic length $\widehat{\rho^*}$ is virtually zero, suggesting the notch stress gradient hardly affects the fatigue resistance. However, since ρ^* basically covers size (i.e. thickness) effects, the limited variation in t_b values (Table 1) could be at least partially responsible for the $\rho^* \to 0$ result, since the notch gradient induced scaling of all S_e values is approximately the same. On the other hand, the confidence bounds (Table 3) indicate that $\rho^* \to t_b$ is not likely, since at the same time the obtained scatter and performance parameter σ has decreased a bit in comparison to the nominal stress based result, introducing the hypothesis that the mode-III fatigue damage process might even be a more near-surface phenomenon than the mode-I process. Experimental results involving t_p values in the range of 5, 15 and even 20 [mm] could help to investigate the validity of this hypothesis. The loading & response ratio coefficient estimate for a local strength criterion like S_e is not different from a global one like S_n: $\widehat{\gamma} \to 1$, suggesting mean (shear) stress hardly affects the mode-III fatigue resistance. Performance parameter σ, the standard deviation, has slightly improved in comparison to the nominal stress based result (Table 3), suggesting that the notch stress gradient contributes at least up to some extent to the effective notch stress performance. However,

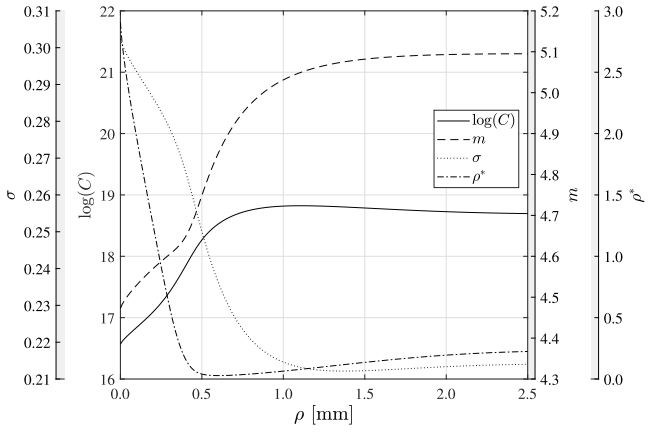

Fig. 25. Most likely parameter estimates as function of adopted real notch radius for specimens with unknown ρ.

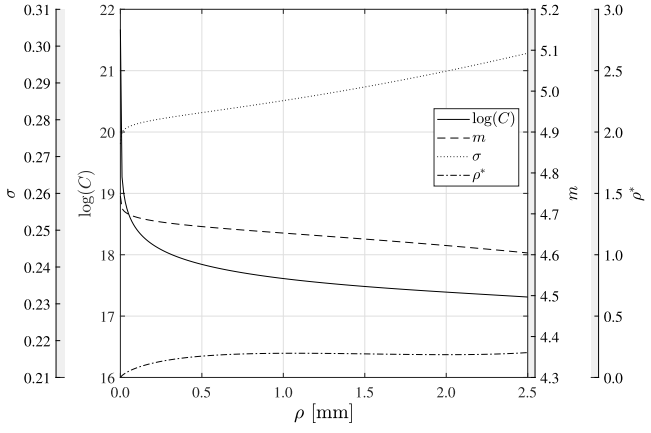

Fig. 26. Most likely parameter estimates as function of adopted real notch radius for all specimens.

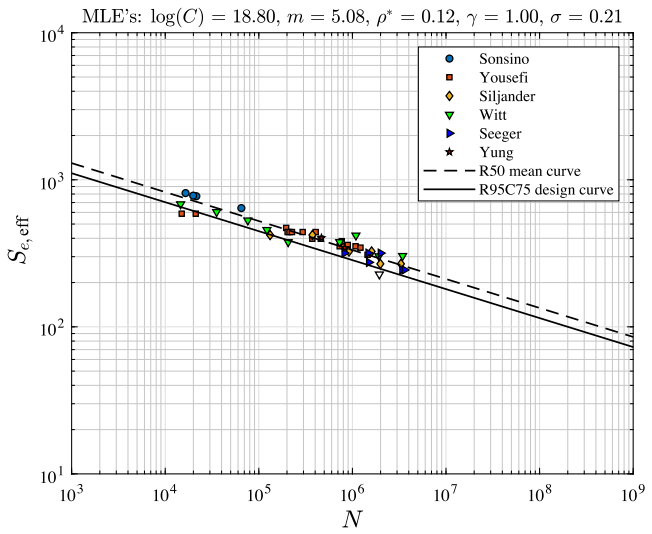

Fig. 27. Effective notch stress based fatigue resistance including mean stress correction for $\rho > 0$.

Table 5
$S_e - N$ normalised co-variance matrix for $\rho > 0$.

Parameter	log(C)	m	ρ*	γ	σ
log(C)	1.00	0.88	−0.25	−0.26	0.24
m		1.00	−0.35	−0.68	0.63
ρ*			1.00	0.49	−0.47
γ				1.00	−0.94
σ					1.00

since the $\rho = 0$ assumption is in conflict with S_e ($\rho^* \rightarrow 0$) estimates, results for $\rho > 0$ needs to be explored.

Real notch radius values are not available for all data sets (Table 1). In order to establish a reasonable ρ estimate, regression analysis results for a range of real notch radii provides insight (Fig. 25). Note that $\gamma = 1$ for all cases. Any $0 \leq \rho \leq 2$ [mm] could be realistic based on the available information (Table 1). Adopting $\rho \sim 1.3$ [mm] seems to provide an optimum, i.e. most likely σ. Using the same ρ value for all data sets (Fig. 26), however, shows that the most likely results are obtained for $\rho \rightarrow 0$. Since $\rho^* \rightarrow 0$ at the same time, results would not improve and $\rho \sim 1.3$ [mm] has been selected as most likely – average – estimate for the data sets with unknown real notch radius.

The $S_e - N$ and parameter profile likelihood plots (Figs. 27 and 28) as well as the normalised co-variance matrix (Table 5) show the analysis results. In comparison to the $\rho \rightarrow 0$ result (Fig. 24 and Table 4), the most likely fatigue strength parameter estimate $\log(\widehat{C})$ has decreased since S_e typically gets smaller for $\rho > 0$. The confidence has increased, mainly as a result of the ρ^* confidence and $\log(C) - \rho^*$ correlation (Table 5), confirming that ρ^* effectively contributes to the fatigue strength characterisation of welded joints, since ρ^* affects S_e and $\log(C)$ accordingly. Damage mechanism parameter, slope $\widehat{m}$, virtually equals the well-known value $m \sim 5$.

The most likely $\widehat{\rho^*} \sim 0.12$ for welded joint mode-III fatigue resistance in steel structures is still relatively small and quite different from the obtained mode-I value: $\widehat{\rho^*} \sim 1.14$ [7], meaning ρ^* would be at least both a material and damage mechanism (i.e. mode) characteristic parameter. The ρ^* confidence is quite large (Table 3). Since physically speaking ρ^* reflects the length in which the majority of the fatigue life has been spent, a relatively small mode-III value in comparison to the mode-I ρ^* supports the hypothesis that the fatigue damage process in mode-III might even be more a near-surface phenomenon than in mode-I. At the same time, the slope m for mode-III is larger than the mode-I value (i.e. $\sim 5 > 3$), meaning the relative contribution of initiation – a (near) surface phenomenon – to the total fatigue life time seems larger for mode-III. Anyway, if ρ^* for mode-III is that small indeed, the real (weld) notch radius stochastics $\rho(\mu, \sigma)$ will be important to capture accurately the zone 2 notch stress gradient. Although a mean stress contribution to the fatigue resistance would seriously affect all parameters, as reflected in the co-variance matrix (Table 5) the stress-relieved and as-welded data does not show any effect, $\widehat{\gamma} \sim 1$ and the confidence is quite large (Table 3). Another local fatigue strength criterion, the Battelle structural stress [39], provides for the same data $\sigma \sim 0.32$ – rather than $\sigma \sim 0.26$ as confirmed by the authors – meaning the effective notch stress performance is much better, since $\widehat{\sigma} \sim 0.21$ and the related scatter index has improved to $T_{\sigma S_e} = 1 : 1.22$.

4. Conclusions

Assuming stress distributions along the expected (2D) crack path are a key element to obtain accurate mode-III fatigue strength and life time estimates, semi-analytical expressions related to the far field stress have been developed for weld toe notches in DS welded T-joints and DS welded cruciform joints, reflecting respectively non-symmetry and symmetry with respect to half the plate thickness. Results for wide range of geometry parameters show an excellent match with solid FE model solutions. For accurate far field stress information, the weld has to be modelled using inclined shell/plate elements. Like for the mode-I formulations, three zones can be identified for all weld notch stress distributions: the zone 1 peak stress value, the zone 2 notch-affected stress gradient and the zone 3 far-field dominated stress gradient, demonstrating stress field similarity.

Taking advantage of the developed semi-analytical weld notch stress distributions, the effective notch stress has been adopted as fatigue strength criterion to establish the welded joint mode-III mid-cycle fatigue resistance characteristics. The involved material characteristic micro- and meso-structural length for mode-III has not been investigated before and the most likely estimate $\widehat{\rho^*} \sim 0.1$ turns out to be different from the mode-I value $\widehat{\rho^*} \sim 1.1$ [7] and is relatively small, meaning ρ^* would be at least both a material and damage mechanism (i.e. mode) dependent parameter. Since ρ^* basically covers size (i.e. thickness) effects, the limited variation in t_b values (Table 1) could be at least partially responsible for $\rho^* \rightarrow 0$, since the notch gradient induced scaling of all S_e values is approximately the same. On the other hand, the confidence bounds indicate that $\rho^* \rightarrow t_b$ is not likely, introducing the hypothesis that the mode-III fatigue damage process might even be a more near-surface phenomenon than the mode-I process. Physically speaking ρ^* reflects the length in which the majority of the fatigue life has been spent, meaning a relatively small mode-III value in comparison to the mode-I ρ^* supports the hypothesis. At the same time, the slope m for mode-III is larger than the mode-I value (i.e. $\sim 5 > 3$), meaning the relative contribution of initiation – a (near) surface phenomenon – to the total fatigue life time seems larger for mode-III indeed. However, since the available amount and variety of data is limited, conclusive answers cannot be provided yet. Anyway, if ρ^* for mode-III is that small indeed, the real (weld) notch radius stochastics $\rho(\mu, \sigma)$ will be important to capture accurately the zone 2 notch stress gradient.

Walker's loading & response ratio coefficient $\widehat{\gamma} \sim 1$, implying that mean stress does not affect the mode-III fatigue resistance. The external loading induced mean shear stress contribution for the considered data sets with $R = \{0, -1\}$ is insignificant and at the same time the contribution of the quasi-constant welding induced residual stress seems negligible as well, since the stress-relieved and as-welded data match the same scatter band. Different mean stress effects have been reported and common denominator seems that for mode-III the mean stress effects are less significant than for mode-I, at least in case more ductile materials like steel are involved. Since $\gamma \sim 0.9$ for mode-I [7,8], the same observation applies to the fatigue resistance of welded joints in steel (maritime) structures.

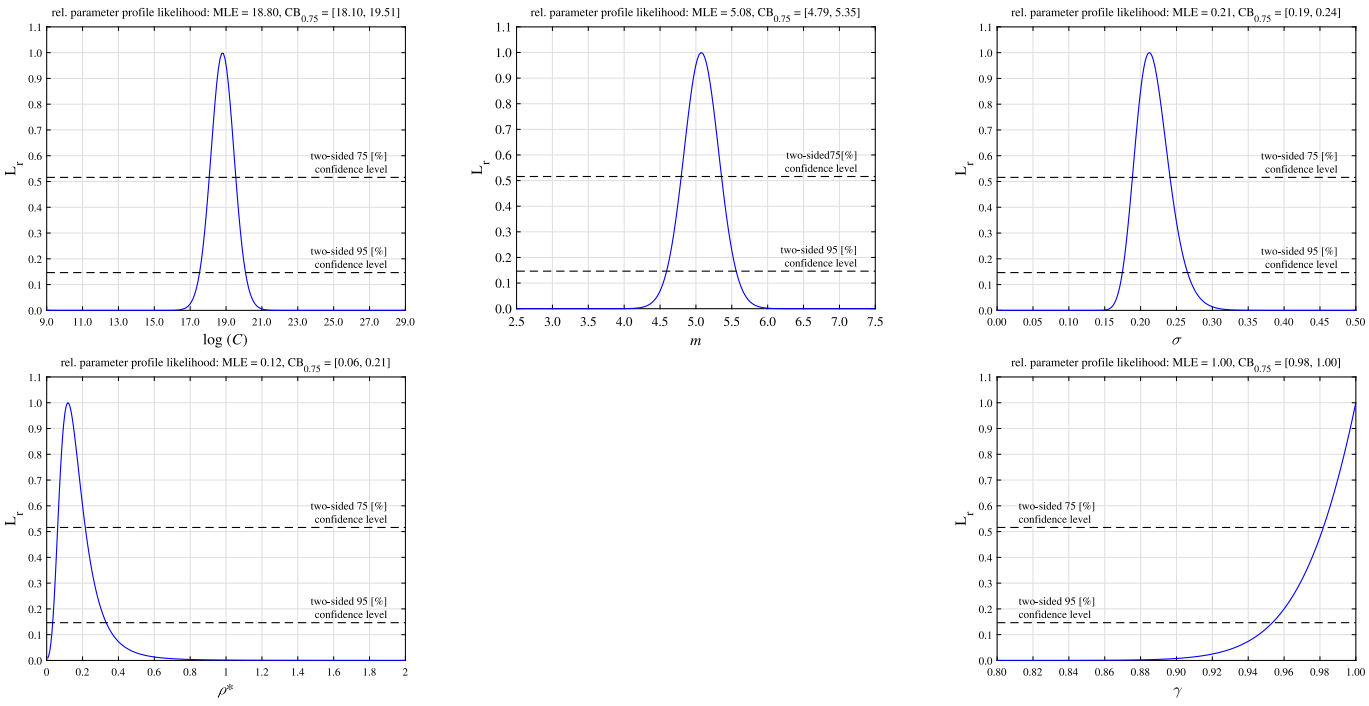

Fig. 28. Effective notch stress based parameter profile likelihood plots including two-sided 75% and 95% confidence bounds for $\rho > 0$.

Declaration of competing interest

The authors declare that they have no known competing financial interests or personal relationships that could have appeared to influence the work reported in this paper.

Data availability

The fatigue resistance data used for model validation is available in literature.

Acknowledgements

The authors would like to thank Koen van Essen for his valuable M.Sc. thesis contribution: "Effective Notch Stress Concept Investigations for Mode-III Loading & Response Conditions", available at repository.tudelft.nl.

Appendix A. Notch stress component formulation

Adopting a complex potential, identically satisfying equilibrium (body forces are assumed to be zero) and compatibility requirements – deformations without any gaps or overlaps, the characteristic stress distribution singularity at a V-shaped notch for a fillet weld geometry with $\rho = 0$ (Fig. 4) can be obtained [18–22]:

$$\tau_{xr}(r,\theta) = C_1 r^{\lambda-1}\sin(\lambda\theta) - C_2 r^{-\lambda-1}\sin(\lambda\theta)$$
$$\tau_{x\theta}(r,\theta) = C_1 r^{\lambda-1}\cos(\lambda\theta) + C_2 r^{-\lambda-1}\cos(\lambda\theta). \quad (A.1)$$

The transformation from Cartesian (Eq. A.1) to Polar coordinates has been obtained using [19]:

$$\tau_{xr} = \tau_{xz}\cos(\theta) + \tau_{xy}\sin(\theta)$$
$$\tau_{x\theta} = \tau_{xy}\cos(\theta) - \tau_{xz}\sin(\theta). \quad (A.2)$$

Boundary conditions to be satisfied at the free surface denote:

$$\tau_{xr}(r,\theta=\alpha) = 0 \quad (A.3a)$$
$$\tau_{x\theta}(r,\theta=\alpha) = 0. \quad (A.3b)$$

Because of symmetry, $\tau_{x\theta}(r,\theta=\alpha) = \tau_{x\theta}(r,\theta=-\alpha) = 0$ is identically satisfied. Substitution of the stress components (Eq. A.1) in the boundary conditions (Eq. A.3) yield:

$$(C_1 r^{\lambda-1} - C_2 r^{-\lambda-1})\sin(\lambda\alpha) = 0 \quad (A.4a)$$
$$(C_1 r^{\lambda-1} + C_2 r^{-\lambda-1})\cos(\lambda\alpha) = 0. \quad (A.4b)$$

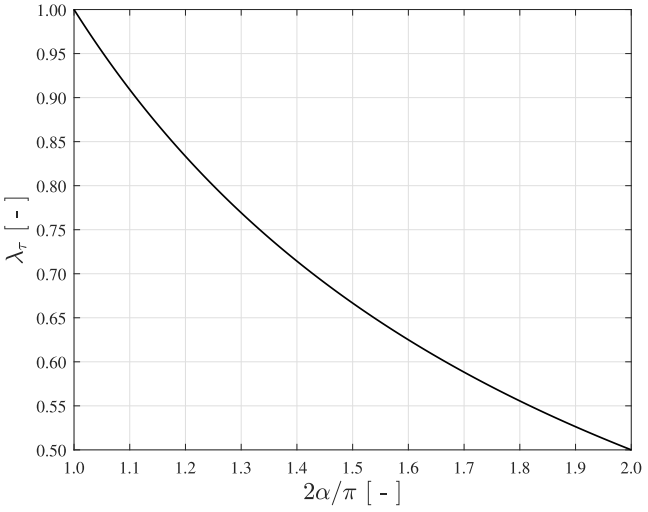

Fig. A.29. Eigenvalue solutions $\lambda_r(2\alpha)$.

Since $(C_1 r^{\lambda-1} + C_2 r^{-\lambda-1}) \neq 0$, the $\tau_{x\theta}$ boundary condition (Eqs. A.3b and A.4b) provides the eigenvalue solution λ:

$$\cos(\lambda\alpha) = 0 \qquad \lambda = \lambda_\tau = \frac{\pi}{2\alpha}. \tag{A.5}$$

Only the first governing notch angle dependent λ_τ, defining the degree of weld notch stress field singularity, will be considered (Fig. A.29). To satisfy the τ_{xr} boundary condition (Eqs. A.3a and A.4a) as well: $\sin(\lambda\alpha) = 0 \rightarrow \lambda = \lambda_\tau = \pi/(2\alpha)$ cannot be satisfied at the same time, meaning:

$$C_2 = C_1 r^{2\lambda}. \tag{A.6}$$

Substitution of C_2 (Eq. A.6) into the stress components $\tau_{xr}(r,\theta)$ and $\tau_{x\theta}(r,\theta)$ (Eq. A.1) yields:

$$\tau_{xr}(r,\theta) = 0 \qquad \tau_{x\theta}(r,\theta) = C_1' r^{\lambda-1}\cos(\lambda\theta). \tag{A.7}$$

Introducing the dimensionless coordinate (r/t_p) as well as τ_s in order to establish a relation to the far field stress (Section 2.3) provides for a weld notch angle dependent stress angle $\theta = \beta$:

$$\tau_{x\theta}\left(\frac{r}{t_p}\right) = \tau_s \left(\frac{r}{t_p}\right)^{\lambda_\tau - 1} \mu_{\tau F}\cos(\lambda_\tau\beta) \tag{A.8}$$

with

$$\mu_{\tau F} = \frac{C_1' t_p^{\lambda_\tau - 1}}{\tau_s}. \tag{A.9}$$

For $\rho > 0$ (Fig. 5), the stress distribution is assumed to be affected for $r \rightarrow 0$ only, suggesting the same complex potential as for $\rho = 0$ can be adopted, but the boundary conditions (Eq. A.3) have to be changed into [22]:

$$\tau_{xr}(r = \rho, \theta) = 0 \tag{A.10a}$$

$$\tau_{x\theta}(r, \theta = \alpha) = 0. \tag{A.10b}$$

Because of symmetry, $\tau_{x\theta}(r, \theta = \alpha) = \tau_{x\theta}(r, \theta = -\alpha) = 0$ is identically satisfied, like for $\rho = 0$. Substitution of the stress components (Eq. A.1) in the boundary conditions (Eq. A.10) yield [22]:

$$(C_1 \rho^{\lambda-1} - C_2 \rho^{-\lambda-1})\sin(\lambda\theta) = 0. \tag{A.11}$$

Since the $\tau_{x\theta}$ boundary condition (Eq. A.10b) for $(\rho = 0)$ and $(\rho > 0)$ is the same, the eigenvalue solution does not change: $\lambda = \lambda_\tau = \pi/(2\alpha)$. However, to satisfy τ_{xr} (Eq. A.10a) requires:

$$C_2 = C_1 \rho^{2\lambda}. \tag{A.12}$$

Substitution of C_2 (Eq. A.12) into the stress components $\tau_{xr}(r,\theta)$ and $\tau_{x\theta}(r,\theta)$ (Eq. A.1) denotes:

$$\tau_{xr}(r,\theta) = C_1' r'^{\lambda_\tau - 1}\sin(\lambda_\tau\theta)\left(1 - (r_0/r')^{2\lambda_\tau}\right)$$
$$\tau_{x\theta}(r,\theta) = C_1' r'^{\lambda_\tau - 1}\cos(\lambda_\tau\theta)\left(1 + (r_0/r')^{2\lambda_\tau}\right). \tag{A.13}$$

Introducing the dimensionless coordinate (r/t_p) as well as τ_s in order to establish a relation to the far field stress (Section 2.3), like for $\rho = 0$, provides for a weld notch angle dependent stress angle $\theta = \beta$:

$$\tau_{xr}\left(\frac{r}{t_p}\right) = \tau_s\left(\frac{r'}{t_p}\right)^{\lambda_\tau-1}\mu_{\tau F}\sin(\lambda_\tau\beta)\left\{1 - \left(\frac{r_0}{t_p}\right)^{2\lambda_\tau}\left(\frac{r'}{t_p}\right)^{-2\lambda_\tau}\right\}$$
$$\tau_{x\theta}\left(\frac{r}{t_p}\right) = \tau_s\left(\frac{r'}{t_p}\right)^{\lambda_\tau-1}\mu_{\tau F}\cos(\lambda_\tau\beta)\left\{1 + \left(\frac{r_0}{t_p}\right)^{2\lambda_\tau}\left(\frac{r'}{t_p}\right)^{-2\lambda_\tau}\right\} \tag{A.14}$$

with

$$\mu_{\tau F} = \frac{C_1' t_p^{\lambda_\tau - 1}}{\tau_s}. \tag{A.15}$$

Appendix B. Weld load carrying shear stress coefficient

To capture C_{tw} estimates, 4th order polynomial fitting functions have been established. In case of non-symmetry:

$$\begin{aligned} C_{tw} = \; & 0.166 + 0.078Q^3P + 0.037WQ^2 - 0.003TWQ^2 - \\ & 0.372P - 0.758QP - 1.517QP^2 + 0.020WQP + \\ & 0.908P^2 + 0.436Q^2P + 0.355Q^2P^2 - 0.024TW^2P - \\ & 2.309P^3 - 0.168WP^3 + 0.004WP + 0.001WQ^2P + \\ & 0.536Q - 0.079WQ + 2.487QP^3 - 0.051WQP^2 - \\ & 0.398Q^2 + 0.179WP^2 - 0.003WQ^3 + 0.012TWQ + \\ & 0.127Q^3 + 0.002W^2P^2 - 0.003W^2Q + 0.016W^2QP - \\ & 0.015Q^4 - 0.019W^2P + 0.003W^3Q + 0.028TQ^2P - \\ & 0.225W + 0.087TP^3 - 0.015TQ - 0.179TQP + \\ & 0.095W^2 + 0.013TQ^2 + 0.271TP + 0.024TWP^2 - \\ & 0.014W^3 - 0.006TW - 0.003TQ^3 + 0.062TWP - \\ & 0.027TWQP - 0.003W^2Q^2 - 0.402TP^2 + 0.301TQP^2 \end{aligned} \tag{B.1}$$

and in case of symmetry:

$$\begin{aligned} C_{tw} = \; & -0.036 - 0.049QP - 0.018Q^2P + 0.087TQP + \\ & 0.257P - 0.035QP^2 + 0.235QP^3 - 0.024T^2WP - \\ & 0.159P^2 + 0.038Q^2P^2 + 0.008T^2Q - 0.004T^2WQ + \\ & 0.599P^3 + 0.047WP^3 - 0.036WQ - 0.022WQP - \\ & 1.619P^4 + 0.006WQ^2 + 0.004T^2Q^2 - 0.036TWP - \\ & 0.012Q - 0.012W^2P^2 - 0.003W^2Q^2 + 0.004TQ^2P + \\ & 0.016Q^2 - 0.084WP + 0.0189W^2P + 0.028WQP^2 + \\ & 0.006T + 0.093TP - 0.102TP^2 + 0.013TQP^2 - \\ & 0.016T^2 + 0.022TQ + 0.016WP^2 + 0.038TWP^2 + \\ & 0.056W - 0.278TP^3 - 0.024TQ^2 + 0.005TWQ - \\ & 0.012W^2 + 0.005T^2P - 0.058T^2P^2 - 0.036T^2QP + \\ & 0.028TWQP - 0.002TW^2 + 0.002T^2W - 0.004TW^2P \end{aligned} \tag{B.2}$$

with

$$T = \log(t_c/2 + l_w)/t_b \qquad W = l_w/h_w \qquad Q = l_w/t_b \qquad P = t_b/R_t. \tag{B.3}$$

Negligible terms are excluded. Fitting function application is not limited to the absolute geometry dimensions as shown (Figs. 10 and 17), but the range for particular relative ones: (l_w/h_w), (l_w/t_b), $\log((t_c/2 + l_w)/t_b)$, (t_b/R_t), has to be satisfied.

References

[1] Schijve J. In: Schijve J, editor. Fatigue of structures and materials. Springer Netherlands; 2009.

[2] den Besten H. Fatigue damage criteria classification, modelling developments and trends for welded joints in marine structures. Ships Offshore Struct 2018;13(8):787–808. http://dx.doi.org/10.1080/17445302.2018.1463609.

[3] Glen I, Dinovitzer A, Paterson R, Luznik L, Bayley C. Fatigue resistant detail design guide for Ship - Ship Structure Committee. In: Ssc-405. U.S. Coast Guard Headquarters; 1999.

[4] Guedes Soares C, Garbatov Y. Marine structures. In: Proceedings of 19th international ship and offshore structures congress, vol. 74. 2015, http://dx.doi.org/10.1016/j.marstruc.2017.09.001.

[5] Van Lieshout PS, Den Besten H, Kaminski ML. Multiaxial fatigue assessment of welded joints in marine structures literature overview of progress in academia and engineering practice. Int Shipbuild Prog 2018;65:29–71. http://dx.doi.org/10.3233/ISP-170141.

[6] Lassen T, Recho N. Proposal for a more accurate physically based S-N curve for welded steel joints. Int J Fatigue 2009;31(1):70–8. http://dx.doi.org/10.1016/j.ijfatigue.2008.03.032.

[7] Qin Y, den Besten H, Palkar S, Kaminski ML. Mid- and high-cycle fatigue of welded joints in steel marine structures: Effective notch stress and total stress concept evaluations. Int J Fatigue 2021;142(July 2020):105822. http://dx.doi.org/10.1016/j.ijfatigue.2020.105822.

[8] Qin Y, den Besten H, Palkar S, Kaminski ML. Fatigue design of welded double-sided T-joints and double-sided cruciform joints in steel marine structures: A total stress concept. Fatigue Fract Eng Mater Struct 2019;42(12):2674–93. http://dx.doi.org/10.1111/ffe.13089.
[9] den Besten J. Fatigue resistance of welded joints in aluminium high-speed craft: a total stress concept (Ph.D. thesis), Delft University of Technology; 2015, p. 1–396.
[10] Neuber H. Kerbspannungslehre. Springer - Verlag; 1937.
[11] Zhang G, Sonsino CM, Sundermeier R. Method of effective stress for fatigue: Part II – Applications to V-notches and seam welds. Int J Fatigue 2012;37:24–40. http://dx.doi.org/10.1016/j.ijfatigue.2011.09.016.
[12] Sonsino CM, Fricke W, De Bruyne F, Hoppe A, Ahmadi A, Zhang G. Notch stress concepts for the fatigue assessment of welded joints - Background and applications. Int J Fatigue 2012;34(1):2–16. http://dx.doi.org/10.1016/j.ijfatigue.2010.04.011.
[13] Radaj D, Lazzarin P, Berto F. Generalised Neuber concept of fictitious notch rounding. Int J Fatigue 2013;51:105–15. http://dx.doi.org/10.1016/j.ijfatigue.2013.01.005.
[14] Carpinteri A, Boaretto J, Fortese G, Giordani F, Iturrioz I, Ronchei C, et al. Fatigue life estimation of fillet-welded tubular T-joints subjected to multiaxial loading. Int J Fatigue 2017;101:263–70. http://dx.doi.org/10.1016/j.ijfatigue.2016.10.012.
[15] Vantadori S, Iturrioz I, Carpinteri A, Greco F, Ronchei C. A novel procedure for damage evaluation of fillet-welded joints. Int J Fatigue 2020;136. http://dx.doi.org/10.1016/j.ijfatigue.2020.105599.
[16] Hobbacher AF. Recommendations for fatigue design of welded joints and components. IIW collection, Springer International; 2016.
[17] CEN. EN 1993-1-9: Eurocode 3: design of steel structures - part 1-9: fatigue. 2005.
[18] Lazzarin P, Filippi S. A generalized stress intensity factor to be applied to rounded V-shaped notches. Int J Solids Struct 2006;43(9):2461–78. http://dx.doi.org/10.1016/j.ijsolstr.2005.03.007.
[19] Lazzarin P, Zappalorto M, Yates J. Analytical study of stress distributions due to semi-elliptic notches in shafts under torsion loading. Internat J Engrg Sci 2007;45(2–8):308–28. http://dx.doi.org/10.1016/j.ijengsci.2007.04.007.
[20] Zappalorto M, Lazzarin P, Yates JR. Elastic stress distributions for hyperbolic and parabolic notches in round shafts under torsion and uniform antiplane shear loadings. Int J Solids Struct 2008;45(18–19):4879–901. http://dx.doi.org/10.1016/j.ijsolstr.2008.04.020.
[21] Zappalorto M, Lazzarin P, Berto F. Elastic notch stress intensity factors for sharply V-notched rounded bars under torsion. Eng Fract Mech 2009;76(3):439–53. http://dx.doi.org/10.1016/j.engfracmech.2008.11.008.
[22] Zappalorto M, Lazzarin P. Stress fields due to inclined notches and shoulder fillets in shafts under torsion. J Strain Anal Eng Des 2011;46(3):187–99. http://dx.doi.org/10.1177/0309324710396019.
[23] Niemi E. Stress determination for fatigue analysis of welded components. Abington in association with the International Institute of Welding; 1995.
[24] Dong P. A structural stress definition and numerical implementation for fatigue analysis of welded joints. Int J Fatigue 2001;23(10):865–76. http://dx.doi.org/10.1016/S0142-1123(01)00055-X.
[25] DNV GL. Class guideline DNVGL-CG-0127: “Finite element analysis”. Oslo; 2016.
[26] Rörup J, Maciolowski B, Darie I. FE-based strength analysis of ship structures for a more advanced class approval. In: PRADS 2016 - proceedings of the 13th international symposium on practical design of ships and other floating structures, no. August 2016. 2016.
[27] Chattopadhyay A, Glinka G, El-Zein M, Qian J, Formas R. Stress analysis and fatigue of welded structures. Weld World 2011;55(7–8):2–21. http://dx.doi.org/10.1007/BF03321303.
[28] Niemi E, Fricke W, Maddox SJ. Fatigue analysis of welded components: designer’s guide to the structural hot-spot stress approach. 2006, p. 1–49. http://dx.doi.org/10.1533/9781845696665.
[29] Aygul M. Fatigue analysis of welded structures using the finite element method. S.l: Lap Lambert academic publ; 2012.
[30] Dong P, Hong JK. The master S-N curve approach to fatigue evaluation of offshore and marine structures. In: 23rd international conference on offshore mechanics and arctic engineering, vol. 2. ASMEDC; 2004, p. 847–55. http://dx.doi.org/10.1115/OMAE2004-51324.
[31] Dong P. A robust structural stress method for fatigue analysis of ship structures. In: Proceedings of the international conference on offshore mechanics and arctic engineering, vol. 3. American Society of Mechanical Engineers Digital Collection; 2003, p. 199–211. http://dx.doi.org/10.1115/OMAE2003-37313.
[32] Sonsino CM, Kueppers M. Multiaxial fatigue of welded joints under constant and variable amplitude loadings. Fatigue Fract Eng Mater Struct 2001;24(5):309–27. http://dx.doi.org/10.1046/j.1460-2695.2001.00393.x.
[33] Yousefi F, Witt M, Zenner H. Fatigue strength of welded joints under multiaxial loading: Experiments and calculations. Fatigue Fract Eng Mater Struct 2001;24(5):339–55. http://dx.doi.org/10.1046/j.1460-2695.2001.00397.x.
[34] Siljander A, Kurath P, Lawrence FV. Non proportional fatigue of welded structures. ASTM Special Tech Publ 1992;(1122):319–38. http://dx.doi.org/10.1520/stp24166s.
[35] Witt M, Zenner H. Multiaxial fatigue behavior of welded flange-tube connections under combined loading. Experiments and lifetime prediction. In: 5th international conference on biaxial/multiaxial fatigue and fracture. 1997, p. 421–34.
[36] Seeger T, Olivier R. Ertragbare und zulaessige schubspanungen schingbeanspruchter. 1987.
[37] Yung, Lawrence F. Predicting the fatigue life of welds under combined bending and torsion. In: Biaxial and multiaxial fatigue. Mechanical Engineering Publications; 1986, p. 53–69.
[38] Bäckström M. Multiaxial fatigue life assessment of welds based on nominal and hot spot stresses (Ph.D. thesis), Laapeenranta University, Finland; 2003.
[39] Mei J, Dong P, Xing S, Vasu A, Ganamet A, Chung J, et al. An overview and comparative assessment of approaches to multi-axial fatigue of welded components in codes and standards. Int J Fatigue 2021;146(November 2020):106144. http://dx.doi.org/10.1016/j.ijfatigue.2021.106144.
[40] Archer R. Fatigue of a welded steel attachment under combined direct stress and shear stress. In: International conference of fatigue of welded constructions. 1987, p. 63–72.
[41] Dekking FM, Kraaikamp C, Lopuhaä HP, Meester LE. A modern introduction to probability and statistics: Understanding why and how. Springer - Verlag London, http://dx.doi.org/10.1198/tech.2007.s502.
[42] Walker K. The effect of stress ratio during crack propagation and fatigue for 2024-T3 and 7075-T6 Aluminum. ASTM Int 1970. http://dx.doi.org/10.1520/stp32032s.
[43] Klassen J, Friedrich N, Fricke W, Nitschke-Pagel T, Dilger K. Influence of residual stresses on fatigue strength of large-scale welded assembly joints. Weld World 2017;61(2):361–74. http://dx.doi.org/10.1007/s40194-016-0407-8.
[44] Findley WN. A theory for the effect of mean stress on fatigue of metals under combined torsion and axial load or bending. J Eng Ind 1959;81(4):301–5. http://dx.doi.org/10.1115/1.4008327.
[45] Nasr A, Nadot Y, Bouraoui C, Fathallah R. Effect of artificial defect and mean shear stress on torsional fatigue behaviour. Appl Mech Mater 2011;146:74–82. http://dx.doi.org/10.4028/www.scientific.net/AMM.146.74.
[46] Pallarés-Santasmartas L, Albizuri J, Leguinagoicoa N, Saintier N, Merzeau J. The effect of mean axial and torsional stresses on the fatigue strength of 34CrNiMo6 high strength steel. In: MATEC web of conferences, vol. 300. 2019, p. 16004. http://dx.doi.org/10.1051/matecconf/201930016004.
[47] Pawliczek R, Rozumek D. Cyclic tests of smooth and notched specimens subjected to bending and torsion taking into account the effect of mean stress. Materials 2020;13(9). http://dx.doi.org/10.3390/ma13092141.
[48] Nishimura Y, Yanase K, Tanaka Y, Miyamoto N, Miyakawa S, Endo M. Effects of mean shear stress on the torsional fatigue strength of a spring steel with small scratches. Int J Damage Mech 2020;29(1):4–18. http://dx.doi.org/10.1177/1056789519831434.
[49] Susmel L. The theory of critical distances: A review of its applications in fatigue. Eng Fract Mech 2008;75(7):1706–24. http://dx.doi.org/10.1016/J.ENGFRACMECH.2006.12.004.